

7

**Insulating Biomaterials**

**Second Quarterly Progress Report**  
**January-March, 1997**

2000

**Submitted to:**

**Neural Prosthesis Program**

**National Institutes of Health**  
**National Institute of Neurological**  
**Disorders and Stroke**

**By the:**

**Biomedical Microelectronics Laboratory**

**Biomedical Engineering Center, Massachusetts Institute of Technology**  
**West Roxbury VA Medical Center**

**Contributors:**

**David J. Edell, PI**

**Karen K. Gleason, Chemical Engineering**

**Bruce C. Larson, Grad Student, Electrical Engineering**

**Scott Limb, Grad Student, Chemical Engineering**

**James R. Mann, Electrical Engineering**

**Terry Herndon**

**Sean Sexton, Electronics**

**Cynthia M. Vanaria, Assembly**

## 1. Instrumentation

### 1.1. High Temperature Soak System Instrumentation

The instrumentation issues associated with the development of the high temperature soak system have been resolved and the first test box has been partially assembled. This test system will have 384 electrometers operating continuously when completed. At present, roughly half of the boards are complete, and the others are awaiting arrival of backordered high value sensing resistors. The system is being operated through HP-VEE (Virtual Engineering Environment) software, and data from the electrometers is being acquired with a Data Translations acquisition board. 64 channel multiplexers are being used to bring the electrometer outputs into the acquisition board. A single D/A converter is being used to supply the voltage sweep. Room temperature and humidity, and heater block temperature is being monitored as well. Many of the initial assemblies had to be rebuilt because the inputs of the electrometers were damaged. This occurred even though the inputs were shorted to the bias line. However, due to a design change, the bias terminal was an open circuit if the output connector was not attached to the multiplexer board. Then, charge could build up on the input stage during cleaning of the circuit boards. Once repaired, the electrometers met design performance.

An open circuit test of the first set of 64 electrometers yielded an average input leakage current reading on the order of 100fA which is due to the offsets of the amplifiers. More importantly, the standard deviation was on the order of 1fA. This should allow reproducible measurement of resistances up to  $10^{15} \Omega$  using a  $\pm 5$  Volt sweep. A set of higher value feedback resistors has been ordered to allow routine measurement of up to  $10^{16} \Omega$ . An intermittent fault is currently occurring in the software or hardware that stops the measurement program. When the problem is solved, this new system will be used to provide continuous measurements of the 90°C test devices, and new test devices for 60°C and 37°C will be constructed of the best materials.

### 1.2. Improved Instrumentation for Animal Measurements

One of the frustrations of prior work has been our inability to reliably monitor the implanted animals. While we know that devices have not overtly failed, we can only make relatively crude measurements because of motion artifacts, and the rapid nature of the required measurement compared to what can be accomplished on the lab bench. In order to improve the measurements, we identified a low power, low input bias current quad operational amplifier that we may be able to assemble into a connector that plugs directly into the animal. This will avoid cable motion problems, and will reduce stray capacitance to a minimum. Reduced capacitance should reduce settling time thereby allowing more accurate measurements within the same time period. If this approach is successful, the portable readout system will be modified to accept the head stage.

## **2. Chip Surface Insulation**

A new series of silicon nitride/silicon dioxide test devices was fabricated this quarter. The previous samples are still under test, but numerous faults such as saline evaporation or leakage, or bias voltage failure occurred during the course of the long term testing occurred which add uncertainty to the overall time course of the failures. The new test sequence will take advantage of the highly reliable long tube configuration and the new silicone materials available for insulating the backside of silicon wafer pieces. Several long term tests of this type of configuration have been made and have shown that surface dielectrics can be tested in this manner.

The test devices are made from bare silicon wafers that have been coated with thin film insulators of interest. The wafers are cut into 13mm squares. Then the backsides are coated with conductive epoxy and a Teflon<sup>®</sup> coated wire is attached. The backside and part of the front except for a circular opening is then coated with a suitable silicone such as Huls PEM25, Factor II 2186, Applied Silicone, or Nusil CF20-2186 so only the exposed test area contacts saline. These devices are then installed into long tubes so that the exposed test areas are under the temperature controlled saline.

The following set of test devices has been fabricated and will be evaluated at 90°C using the new test system. There are four of each type in each long tube.

1. 1,000A LPCVD silicon nitride on bare silicon.
2. 5,000A PECVD silicon nitride on bare silicon.
3. 1,000A LPCVD silicon nitride over 1,000A thermal oxide.
4. 5,000A PECVD silicon nitride over 1,000A thermal oxide.
5. 5,000A LTO deposited oxide over 1,000A LPCVD silicon nitride on bare silicon.
6. 5,000A LTO deposited oxide over 5,000A PECVD silicon nitride on bare silicon.
7. Bare silicon coated with Nusil CV2500 for a control.

## **3. Surface Interface Protection**

A new triple track device was assembled using Nusil Med-4-4220 silicone in a side by side pack. This material has good handling properties, traps few bubbles, is optically clear, and has good tear strength. While the Nusil CF20-2186 material is similar, the Med-4-4220 material falls within their medical products line and is thus more attractive for this work. The new device will be placed under test at 90°C in saline.

## **4. Wire Insulation**

Wire spools of BioKote coated platinum wire from PI Medical, spools of Teflon<sup>®</sup> coated 1 mil platinum-iridium wire from AM Systems, and spools of Isonel coated 1 mil platinum wire from AM Systems were fabricated and placed under soak. The Teflon<sup>®</sup> coated wire failed instantly. Microscopic evaluation revealed numerous pinholes in the

film. Other Teflon<sup>®</sup> coated wires with thicker, pinhole free coatings continue to test well. Preliminary results with BioKote and Isonel are promising.

### **5. Fluorocarbon Research**

A matrix of deposition parameters for improving fluoropolymer deposition rates has been completed and is now under evaluation. Fluoropolymer samples on wires and silicon chips have been soak tested but have performed poorly. Small pin holes in the films seem to be responsible for the failures, but further evaluation is needed. Triple track devices failed very rapidly, apparently due to delamination of the film which was not unexpected. These tests provide baseline data for testing adhesion promotion ideas, and for evaluation of the higher deposition rate films in the future. A paper on the fluorocarbon chemistry research is appended to this progress report.

### **6. Animal Implants**

Animal implant work has focused on development of a skull mount device for long term testing of devices in the subdural space. We have been testing bone cement/acrylic cement composit assemblies with good success. 3M company has provided us with samples of new composit acrylic cement materials that are promising. We still plan to use Microtech connectors for the initial implants, but due to the solvent expansion problem associated with silicones, the connector/wire interface will be epoxy encapsulated. This should remain reliable since most of the epoxy will be exposed to air rather than tissue. Devices with simple loops of Teflon<sup>®</sup> coated platinum-iridium wire will be fabricated and implanted next quarter. New connectors have been ordered from Molex but have not yet arrived. These new connectors should allow smaller head assemblies with very low profiles compared to the Microtech connectors.

### **7. Flexible Circuit Materials Evaluation**

Kapton ribbon cables with interdigitated electrodes have been received and placed under test. Three sets have been tested so far with silicone encapsulation: bare Kapton, acrylic coated Kapton with silicone overcoat, and a Kapton/acrylic/Kapton sandwich structure with no overcoat. All three sets have exhibited relatively high leakage currents, and most have failed within a few days after immersion in 90°C saline. Several epoxies and acrylic encapsulants are being considered to solve this problem. Also, the epoxy coated Kapton samples should be available next quarter.

One difficult problem to solve with the Kapton/silicon assemblies is the protection of both the silicon dioxide surface and the Kapton surface. While we can find materials that may protect the Kapton surface such as acrylic adhesives or epoxies, these will not likely work with the silicon surface. However, the silicon surface can be protected with silicones. Perhaps we will find one material that does both, but more likely we will rely on protecting the bonds with an acrylic or epoxy, and the silicon with silicone. This will leave an interface between the silicone and the epoxy that may be difficult to protect. We are working on this problem in collaboration with the University of Michigan.

6-2970

# Pulsed Plasma Enhanced Chemical Vapor Deposition from Hexafluoropropylene Oxide: Deposition Behavior and Modeling Study

Scott J. Limb<sup>1</sup>, David J. Edell<sup>2</sup>, Edward F. Gleason<sup>3</sup>, and Karen K. Gleason<sup>1</sup>

<sup>1</sup>Department of Chemical Engineering, MIT

Cambridge MA 02139

<sup>2</sup>Division of Health and Sciences, Harvard University

Cambridge MA 02139

<sup>3</sup>MIT Lincoln Laboratory

Lexington MA 02173

SUBMITTED TO:

"CHEMISTRY OF MATERIALS"

## ABSTRACT

Pulsed plasma enhanced chemical vapor deposition(PECVD) from hexafluoropropylene oxide was investigated using a radio frequency (rf) parallel plate reactor. Deposition kinetics were experimentally determined as a function of plasma processing conditions including on-time, off-time, pressure, flow rate, substrate temperature, electrode spacing, and substrate potential. Corresponding film compositions were measured by x-ray photoelectron spectroscopy. As compared to continuous rf PECVD, pulsed excitation increases the  $\text{CF}_2$  fraction in the film. Varying the pulse cycles resulted in good control over film composition with high  $\text{CF}_2$  fraction films of 65% depositing at low pulse cycles. All films had  $< 2$  atomic% oxygen. The deposition per cycle as a function of off-time increased monotonically until a plateau region was reached indicating depletion of the reactive gas-phase precursors. Increasing pressure, flow rate, electrode spacing, off-time, on-time, and decreasing substrate temperature resulted in higher deposition rates. Furthermore, a simplified model of the thickness deposited during each cycle was developed and the effect of homogeneous recombination was found to be statistically significant. The precursor adsorption was found to be the rate limiting process at high temperatures. An apparent negative activation of  $-3.90 \pm 0.11$  kcal/mol for the surface deposition rate constant was found. Furthermore, model parameters predicted a low combined sticking coefficient for  $\text{CF}_x$  species of  $1.7 \times 10^{-3}$  unto a fluorocarbon layer.

# I. Introduction

Plasma enhanced chemical vapor deposition (PECVD) is frequently used in microelectronics processing. Films can be electrically insulating, pinhole free, conformal, excellent permeation barriers, sterile upon deposition, and can be deposited onto a variety of different substrates.<sup>1</sup> In particular fluorocarbon PECVD has been explored as a possible means of depositing films similar to bulk polytetrafluoroethylene (PTFE,  $(\text{CF}_2)_n$ , Teflon<sup>TM</sup>). Bulk Teflon<sup>TM</sup> has many remarkable properties, including a low dielectric constant of 2.1,<sup>2</sup> low coefficient of friction between 0.05 and 0.08,<sup>3</sup> low permeability constant,<sup>3</sup> and biocompatibility.<sup>4-6</sup> This motivates the desire to produce thin film coatings having similar composition and properties. The electrical properties of bulk PTFE makes it an excellent candidate for an interlayer dielectric. Also, the known biocompatibility of bulk Teflon<sup>TM</sup>, suggests these coatings could be used in a variety of biomedical applications including lead wires for pace makers, catheter inserts, neural probes, and implantable tubing.

Although there are several treatises detailing the extensive research into the PECVD of fluorocarbon thin films,<sup>7-10</sup> the majority of these studies used continuous radio-frequency(rf) PECVD within the glow region. The majority of the plasma process conditions investigated resulted in PECVD films differing in composition from that of bulk PTFE. Studies included deposition from fluorinated ethylenes such as  $\text{C}_2\text{FH}_3$ ,  $\text{C}_2\text{F}_2\text{H}_2$ ,  $\text{C}_2\text{F}_3\text{H}$ , and  $\text{C}_2\text{F}_4$ ,<sup>11</sup> and saturated fluorocarbons, such as  $\text{C}_n\text{F}_{2n+2}$  ( $n = 1, 2, 4, 6$ ,

8).<sup>12</sup> The effects of power, pressure, and flow rate were also investigated for  $C_2F_4$  plasma depositions<sup>13</sup> along with rf biasing.<sup>14</sup> Furthermore, the effect of substrate temperature on plasma polymerization was researched.<sup>15</sup> A typical F/C ratio for films deposited under these various process conditions is only ~1.6. Also, the carbon-1s X-ray photoelectron spectroscopy (XPS) reveals that in addition to  $CF_2$  groups, comparable concentrations of  $CF_3$ , CF and quaternary carbon moieties ( $\underline{C}$ -CF and carbon with no  $\beta$  substituted fluorine) are also found in continuous PECVD materials. The CF and  $\underline{C}$ -CF groups are potential sites of crosslinking within the polymeric film. Reducing crosslinking is critical in achieving flexible coatings.<sup>16</sup> Unlike bulk PTFE, continuous PECVD films may contain carbon-carbon double bonds.<sup>17, 18</sup> In one study, while obtaining higher crosslinked plasma polymers within the glow region, researchers demonstrated the deposition of films with few crosslinks and high  $CF_2$  fractions downstream from the glow discharge, but deposition rates were low.<sup>19, 20</sup> Lastly, in the presence of  $H_2$ , variable power studies of  $C_2F_6$  plasma have deposited materials ranging in  $CF_2$  content from 53% to 8%.<sup>21, 22</sup> At the early stage of growth(i.e. after one short rf pulse), the film deposited contained 100%  $CF_2$  species. This work showed promise for high  $CF_2$  content materials that can be deposited via single pulsed deposition.

Pulsed PECVD has shown promise in molecularly tailoring the resulting film composition in order to deposit films similar to bulk PTFE in composition.<sup>23</sup> In these depositions, the applied power is pulsed rather than continuously applied. Studies depositing fluorocarbons using short pulses (<1 ms) have been investigated.<sup>24</sup> More

recently, results from longer pulse on-times (~10 ms) have been reported.<sup>16, 23</sup> During the pulse, the substrate is exposed to the glow discharge which is comprised of ions, electrons, excited species, and neutrals. In the off-time between the pulses, the long lived neutral intermediates dominate.<sup>25</sup> The pulsing process is related to remote or afterglow PECVD,<sup>26</sup> where the substrates are placed outside the glow region. Although both pulsed and downstream PECVD allow long lived neutral intermediates to be involved in the deposition process, only the pulsed PECVD allows for ion bombardment of the substrate. In addition, transport of the reactive gas phase species to the growth surface is simpler for pulsed PECVD than for the downstream configuration. In addition, pulsed rf discharges have been used to study the plasma kinetics as the dynamic process gives direct information on the rates of chemical and physical phenomena in the plasma.<sup>25</sup> Control of film properties and deposition rates,<sup>27</sup> uniformity,<sup>28</sup> and etching<sup>29</sup> have been investigated by power modulation.

Work by Savage and coworkers<sup>23</sup> on pulsed PECVD using hexafluoropropylene oxide (HFPO) as a monomer has produced results where the films deposited on planar silicon wafers were similar to bulk PTFE in composition. In their work, the substrates were held at a floating potential in a 10-cm diameter, 30.5-cm long Pyrex glass cylindrical reactor. The rf power was provided by external concentric metal rings located at both ends of the reactor vessel. Deposition rates and  $CF_x$  content were determined at various pulse on-times and off-times at a pressure of 430 mtorr. The average deposited thickness during a pulse increased as the off-time increased until a plateau was reached. Also,  $CF_2$

contents as high as 80% were attained. Pulsed work has also shown similar results from  $\text{CF}_4$  and  $\text{C}_2\text{F}_6$  gases with  $\text{H}_2$  addition.<sup>30</sup>

In this paper, more extensive studies of pulsed PECVD from HFPO are reported and a model of the deposition process is developed. Models of the plasma physics, chemistry, and surface deposition during a continuous plasma<sup>31-33</sup> exist but provide limited information for pulsed plasma systems. One analysis of a generic pulsed PECVD reactor with recycle<sup>34</sup> has been studied with deposition and uniformity modeled as a function of reactor operating conditions. Unlike the model to be described here, gas-phase addition reactions were neglected. Thus, it is limited to low concentrations of reactive species (i.e. low pressure and power). Also, comparison to experimental data was not made. In this work, experimental deposition rate and film composition at various reactor operating conditions including pressure, flow rate, substrate potential, substrate temperature, and average input power will be compared to model predictions in order to provide a better understanding of pulsed PECVD from HFPO. Furthermore, two models, one with gas-phase addition reactions and the other without will be compared to experimental data.

## II. Experimental

### A. Plasma Apparatus and Operating Conditions

A schematic diagram of the pulsed PECVD reactor (20-cm diameter, 8-cm high stainless steel chamber) used in this work is shown in Fig. 1. Two ports are available for feedthroughs and pump connections. The powered electrode (11.4-cm diameter aluminum disk) and grounded electrode (11.4-cm diameter aluminum cylinder) are spaced 1 inch apart with samples placed on the grounded electrode. The total reactor volume excluding the electrode volume is  $5100 \text{ cm}^3$  and the effective volume in-between the two electrodes is  $261 \text{ cm}^3$ . The applied rf is delivered by a 13.56 MHz power source (ENI Power System, Inc., model HF-300T). This amplifier delivers a maximum of 280 W. Its power output can be controlled with a 0-10 volt input. For pulsing, the rf power is modulated using a pulse generator (Systron-Donner Corporation, Datapulse 100A). An oscilloscope is used to calibrate the pulse duration.

PECVD was accomplished by flowing undiluted HFPO (from PCR Inc., 99% purity) into the parallel plate reactor. The gas flowed through a showerhead configured in the powered electrode. The gas flow rate was metered into the reactor by mass controllers (Tylan FC-280) with a 0-40 sccm (STP) range. The pressure in the system was monitored by a pressure transducer (MKS Baratron, model 222c) and controlled with a butterfly valve (Vacuum General, Model MDV-D15) connected in a feedback loop to the pressure controller (Vacuum General, Model 80-2). Impedance matching was accomplished with a LC network (Heath Company, model SA-2060A).

Silicon wafer substrates were employed for XPS and ellipsometry measurements. Unless otherwise stated, the wafers were placed on the grounded electrode. Besides the grounded electrode, silicon wafer substrates were also placed on 1/4 inch thick glass plates having the same areal dimensions as the substrates. The glass plates were on the grounded electrode and allowed for the silicon wafer substrates to be electrically isolated.

Reactor pressures of 1.2, 1.0, 0.75, and 0.40 torr were used along with HFPO flow rates of 23, 12.5, 5.1 sccm (STP). The rf power source was pulsed by varying on-time from 1 to 150 ms and off-times from 10 to 2000 ms. When continuous rf excitation was used, the power was set at either 280 W or 50 W. The 50 W power setting was required to achieve deposition because at the higher power (280W), etching occurs. For pulsed PECVD, the peak power was fixed at 280 W. Unless otherwise noted, substrate temperature was maintained with the grounded electrode at  $293 \pm 3$  K with backside water cooling.

Experiments at substrate temperatures ranging from 235 to 396 K were performed either by cooling the grounded electrode with cold nitrogen gas or by resistively heating an electrically grounded aluminum plate on the grounded electrode. In Fig 1b. the resistively heated plate has a Chromalox heating element on the backside with a thermocouple in the center of the electrode. The variable temperature experiments were at 1 torr with flow rate at 12.5 sccm HFPO and substrates placed on the heating plate.

## **B. Deposited Film Analysis**

The analytical techniques employed for the investigation of deposition rates and materials characterization were ellipsometry and X-ray Photoelectron Spectroscopy

(XPS). Film thickness and index of refraction were attained from an ellipsometer (Gaertner L116A) with a helium-neon laser having a beam wavelength of 6328 Å. The polarizer was set at 45° and the angle of incidence at 70°. The XPS spectrometer (Perkin Elmer 5100) employed a monochromatic Mg  $K\alpha_{1,2}$  exciting radiation source. The Mg anode X-ray source was operated at 300 W with a pass energy of 17.9 eV for the carbon 1s (C1s) spectra and a pass energy of 178.95 eV for the survey scans. The angle between the X-ray source and the analyzer was set at 45°. Charging effects up to 3 eV were corrected for by referencing the extraneous hydrocarbon contamination peak to 294 eV and by comparing the F/C ratios obtained by the survey scans to those calculated from C1s spectra. The samples were not sensitive to X-ray damage as minimal changes were seen after a 45 min exposure time. Only a 10 min exposure time was required to obtain the C1s spectra. For reference, C1s spectra was also taken of a bulk PTFE sample.

Deconvolution of the XPS line shapes was performed using the Perkin Elmer 5100 software which incorporates an intensive volume of background data for binding energies. Good correlation between the predicted and experimental spectra was gathered assuming 60/40 Gaussian/Lorentzian line shapes with the full width at half-maximum of each lineshape set at 2 eV. The bulk PTFE C1s spectra were resolved using a full width at half-maximum at 1.7 eV.

### III. Results and Discussion

#### A. Pulsed and Continuous Plasma.

Unless otherwise noted, the reactor conditions used appear in Table 1. Also, for the deposition per cycle figures, both the experimental data and model predictions are plotted. The experimental data marked by symbols will be discussed in section III while the model predictions marked by either a dashed or solid line will be discussed in section V. Furthermore an average value for the deposition per cycle was calculated by dividing the overall film thickness by the number of rf cycles used during the deposition time.

Fig. 2 compares the carbon 1s XPS spectra for continuous and pulsed rf excitation for PECVD. The pulsed PECVD film (Fig. 2b) was deposited using a 10 ms on-time / 400 ms off-time (10/400) duty cycle. Deconvolution shows features assigned as  $\text{CF}_3$  (294 eV),  $\text{CF}_2$  (292 eV),  $\text{CF}$  (289.5 eV),  $\underline{\text{C}}\text{-CF}$  (287.3 eV).<sup>8</sup> The  $\text{CF}_2$  percentage obtained by pulsing, 62%, is substantially higher than for the traditional PECVD deposited at 50W peak power, 32%. Integration of the  $\text{CF}_3$ ,  $\text{CF}_2$ ,  $\text{CF}$ , and  $\underline{\text{C}}\text{-CF}$  components allows a F/C ratio to be calculated from the C1s spectra. For the continuous PECVD films (Fig. 2a), this calculation gives a F/C value of 1.55. For the pulsed PECVD film (Fig. 2b), the F/C ratio is 1.80. For both films, the F/C ratio calculated from the C1s spectra agrees to within 5% of the value measured by the XPS survey scan.

The percentages of  $\text{CF}_3$ ,  $\text{CF}$ , and  $\underline{\text{C}}\text{-CF}$  in Fig. 2a are comparable. The same is true for Fig. 2b and is a typical characteristic of the spectra of all fluorocarbons deposited in this work. Hence, only one number, the  $\text{CF}_2$  percentage, will be used to qualitatively

describe the carbon-1s XPS results. The  $\text{CF}_2$  fraction is also an important figure of merit for the films relative to bulk PTFE (100%  $\text{CF}_2$ ). For all the films in this study, XPS survey scans show the oxygen content is less than 2 atomic%. This indicates that little oxygen from the HFPO precursor is being incorporated into the film. In addition, some or all of the incorporated oxygen impurities may result from atmospheric exposure.

In order to discuss these results, the fluorocarbon plasma chemistry occurring during the on-time will be grouped into the following reactions:



Reaction 1 has been observed via thermal and plasma excitation as primary decomposition pathway for HFPO at low pressure.<sup>35</sup> Recently, our group has shown this same mechanism can explain the activation energy observed for thermal CVD from HFPO.<sup>36</sup> We hypothesize this pathway is also important for pulsed PECVD. In support of this idea, note that the low oxygen content of the pulsed PECVD films is consistent with the majority of the oxygen leaving the reactor in the form of the ketone or the likely decomposition products of reaction 3, CO and COF. In addition, the production and subsequent polymerization of difluorocarbene ( $\text{CF}_2$ ) would incorporate  $\text{CF}_2$  units into the film.

Two factors are anticipated to be important for depositing films with high  $\text{CF}_2$  percentages. First, the gas-phase mole fraction of  $\text{CF}_2$  relative to other film forming fluorocarbon species,  $\text{CF}_3$  and CF, must be high. Thus, reactions 2, 3, and 4 must be

minimized. Second, once deposited,  $\text{CF}_2$  groups in the film must be protected from further surface reactions initiated by energetic bombardment and chemical etching. Fluorocarbon plasma produce light, electrons, ions, and reactive neutrals which effect the growing surface. Indeed, ion bombardment,<sup>37</sup> x-ray,<sup>38</sup> electron irradiation,<sup>39</sup> and fluorine atoms<sup>40</sup> are capable of altering the surface of bulk PTFE and lowering the  $\text{CF}_2$  fraction. Presumably similar processes occur during fluorocarbon deposition. The competition of such "etching" processes with film growth is a well established paradigm in the plasma CVD literature.<sup>8</sup>

Pulsed plasma excitation could effect the gas phase composition in the reactor, the ion bombardment of the growing surface or both. Undesired processes, such as rxns. 2 and 3, which create gaseous precursors other than difluorocarbene, are more likely the greater the number of pulsed excitation periods a gas-phase molecule experiences before flowing out of the reaction zone. This plasma exposure time depends on both the duty cycle of the pulse excitation and the residence time of the reactor. In addition, varying the duty cycle will alter the exposure of depositing material to the glow discharge, especially to the effect of ion bombardment.

In order to investigate the effect of reducing the average ion bombardment energy, substrates were placed on an electrically isolated glass plate. All other conditions were the same for the pair of films discussed for Fig. 2. Fig. 3 shows the resulting  $\text{C1s}$  XPS spectra. Comparing Fig. 2a and Fig. 3a for the continuous PECVD, the  $\text{CF}_2$  percentages are found to be identical. However, there is slightly less intensity in the defluorinated

species, CF and CF<sub>2</sub>, for the isolated substrate. The results support the hypothesis that energetic ion bombardment leads to defluorination of the growing surface. In contrast, for the 10/400 case, Fig. 2b and Fig 3b show virtually indistinguishable spectra. Thus, at the low duty cycle associated with the 10/400 pulse conditions, the fraction of growing surface exposed to ion bombardment is small. Also, the similarity of Figs. 2b and 3b confirms that gas phase chemistry is not perturbed by the addition of the glass plate under the substrate.

### B. Off-times

As off-time is increased, the deposition per cycle increases monotonically until a plateau is reached after approximately 200 ms (Fig. 4a). This behavior is in qualitative agreement with results reported previously by others.<sup>23</sup> The plateau corresponds to a maximum deposition per cycle of  $1.8 \pm 2 \text{ \AA}$ . In this region, additional film growth does not result as off-time is increased, indicating depletion of the reactive gas-phase precursors which were generated during the on-time.

At an off-time of zero, corresponding to continuous 280 W rf excitation, no net deposition was observed onto a silicon substrate. Furthermore, fluorocarbon films exposed to this continuous plasma were etched. The loss in thickness was used to calculate the deposition per cycle value of  $-0.18 \text{ \AA}$  which appears at zero off-time in Fig. 4a. This observation suggests that net etching may also be occurring during the 10 ms on-time.

Figure 4b shows the %CF<sub>2</sub> as a function of off-time. This graph displays the same trend as was observed in the deposition per cycle results (Fig. 4a). The %CF<sub>2</sub>

increases with off-time until a maximum value of 65% is reached. Variation in the off-time from 400 to 2000 ms produces little change in the %CF<sub>2</sub>. The data at zero off-time in Fig. 4b does not represent the standard power of 280 W. As mentioned above, no film deposits under these conditions. Instead the data at zero off-time is the %CF<sub>2</sub> in a film deposited at 50 W.

Increasing off-time while holding on-time fixed decreases both the fraction of time the gas-phase is subjected to plasma excitation and the fraction of time the growing film is exposed to ion bombardment. Reduced plasma excitation of the gas may limit undesirable fragmentation reactions (Eq. 2-4), thus increasing the concentration of CF<sub>2</sub> in the gas phase. Reduced ion bombardment may limit undesired defluorination reaction of the surface. Both effects could contribute to the observed increase in %CF<sub>2</sub> in the deposited film.

### C. Pressure

At other pressures, similar trends in deposition per cycle and %CF<sub>2</sub> are observed as a function of off-time. In Figure 5a, the same monotonic increase in deposition per cycle with off-time are seen until a plateau is reached. However, maximum deposition per cycle increases as pressure is increased. At 400 ms off-time, plateau thicknesses are 0.25 Å at 400 mtorr, 1.4 Å at 750 mtorr, 1.8 Å at 1000 mtorr and 2.2 Å at 1200 mtorr. The deposited thickness in the plateau region are roughly proportional to pressure (Fig. 5b). Furthermore, the deposition per cycle is also nearly linear with pressure at shorter values of off-time. For instance, Fig. 5b also shows the deposition per cycle at a fixed off-time of 20 ms.

C1s XPS spectra show that %CF<sub>2</sub> as a function of off-time at 750 and 1200 mtorr is indistinguishable from the results at 1000 mtorr(Fig. 4b). However, at 400 mtorr, 43% and 49% CF<sub>2</sub> content were observed at the 200 ms and 400 ms off-times respectively. Thus, from 1000 mtorr to 400 mtorr, %CF<sub>2</sub> decreased by as much as 16% at 400 ms off-time. This indicates that greater gas phase fragmentation and surface interaction defluorination may be occurring resulting in lower film CF<sub>2</sub> composition. Decreasing the pressure increases both the average electron energy and mean free path. Increasing the average electron energy may increase the rate of fragmentation processes(Eq. 2-4). Thus the gas phase concentration of CF<sub>2</sub> will decrease. Longer mean free paths could increase the energy of the ion bombardment and the higher energy may be sufficient to cause significant surface defluorination.

#### **D. Flow Rate**

The observed plateau in deposition per cycle (Fig. 4a) could simply result from convective loss of activated precursors from the reactor. To test this hypothesis, mean residence time was varied by changing flow rate while holding all other process conditions fixed. By lowering the flow rate, convective loss should become less significant. Fig. 6 shows that decreasing the flow rate from 23 to 12.5 sccm does not significantly effect the deposition per cycle as a function of off-time. In addition, XPS data show that the %CF<sub>2</sub> as a function of off-time is similar for these two flow rates. Thus, in this relatively low flow rate regime, convective loss is not the dominate cause of the observed plateau. This agrees with expectation, as the calculated residence time for the base conditions(Table 1)

is longer than the off-time required to reach the plateau region (approximately 200 ms). It is anticipated at higher flow rates, convective loss could become a significant factor.

At very low flow rates, the residence time becomes long with respect to overall cycle time. Fig. 6 shows the deposition per cycle is smaller using 5.1 sccm as compared to the 12.5 or 23 sccm. In addition, %CF<sub>2</sub> at 400 ms off-time is also lower at 55%. These effects may be caused by undesirable fragmentation reactions (Eq. 2-4) occurring to a larger degree when subsequent excitation periods occur before reactive precursors and fragments created by the previous pulse can exit the reactor.

#### **E. Substrate Temperature**

In Figure 7a, deposition per cycle is plotted as a function of substrate temperature at flow rates of 23 sccm (open symbols) and 12.6 sccm (filled symbols). Because very little difference between these two flow rates were observed in Fig. 6 and in the %CF<sub>2</sub> data, the data at 23 and 12.5 sccm were combined in Fig. 7a. Deposition per cycle increased from 0.4 to 2.6 Å with decreasing substrate temperatures from 126 °C down to -26 °C. An Arrhenius plot (Fig. 7b) shows an apparent negative activation energy which is indicative of an absorption limited process.<sup>41</sup> Leveling off of the data at lower substrate temperatures may be an indication that the rate is becoming mass transport limited.<sup>42</sup>

C1s XPS spectra show that %CF<sub>2</sub> was 62% ± 3% for substrate temperature from -26 °C to 69 °C. A slightly lower value of 55% was measured at 126 °C. Thus substrate temperature had minimal effect on the film composition even though deposition rate

changed dramatically from 0.4 to 2.6 Å/cycle. The similar %CF<sub>2</sub> in the films suggest, not surprisingly, that gas phase chemistry is relatively unaffected by substrate temperature. Earlier(Fig. 3) ion bombardment was shown to have minimal effect at a 10/400 pulse cycle. The lower %CF<sub>2</sub> at 126 °C may indicate ion bombardment effects becoming relatively more important when film growth becomes slow. A low deposition rate results in a higher fraction of film exposed to ion bombardment. Because the percentages of CF, CF<sub>2</sub> and CF<sub>3</sub> did not vary strongly with substrate temperatures, the sticking coefficients of CF<sub>x</sub> species must follow similar functional dependence on substrate temperature. Furthermore, note that films with high CF<sub>2</sub> fractions were deposited at high substrate temperature. Such films are likely to have improved the thermal stability compared to films deposited at lower substrate temperatures.

Figure 8 shows the deposition per cycle for varying off-times at 70°C substrate temperature. The higher substrate temperature lowered the maximum deposition per cycle thickness but trend is similar to the room temperature data(Fig. 4a). The lower deposition rate at higher substrate temperature was anticipated from the apparent negative activation energy shown in Fig. 7b.

#### **F. Electrode Spacing**

In Figure 9, deposition per cycle data as a function of off-time is plotted for an electrode spacing of 1/2 inch (12.5 sccm) and 1 inch (23 sccm). The lower electrode spacing decreases the maximum thickness per cycle but similar monotonic increases in deposition per cycle is observed compared to the 1" spacing data(Fig. 4a). Also, a decrease in spacing of 1/2 resulted in a deposition per cycle decrease of about 1/2 from

1.8 Å to 0.97 Å at a 400 ms off-time. This change in thickness may be due to the effective reactor volume in between the electrodes changing without significant variation in the plasma concentration. Because the plasma is not well confined in-between the electrodes, the overall plasma volume would be large compared to the volume of the electrode gap. In this limit, a decrease in the electrode gap would have minimal effect on the total plasma volume and hence the plasma concentrations should also remain relatively unchanged.

With the decrease in electrode spacing, the % CF<sub>2</sub> in the deposited film decreased from 63 ± 2 % to 50% for the 400 ms off-time deposition. The decrease in %CF<sub>2</sub> may be due to the lower deposition thickness. Having a lower deposition per cycle results in a larger fraction of the film being exposed to the plasma which will increase the undesired defluorination of the surface.

#### **G. On-Time**

In Figure 10a and 10b, deposition thicknesses and %CF<sub>2</sub> in the films respectively are plotted as a function of on-time while holding the off-time constant at 400 ms and flow rate at 12.6 sccm. As on-time is increased from 10 ms to 150 ms, the deposition per cycle increased from 1.7 Å to 6.4 Å. Since it is assumed that a steady state concentration has not been reached within 10 ms, a longer on-time may result in greater gas-phase concentration of CF<sub>x</sub>. This increased may produce significant deposition during the on-time and increase the deposition rate during the off-time. Furthermore, it was previously mentioned that net etching occurred during a continuous plasma at 280 watts. Thus, as

on-time goes to a large number compared to the off-time, the deposition per cycle may decrease and eventually approach the continuous plasma results.

In Fig. 10b, evidence of greater surface defluorination and gas phase fragmentation are shown in the %CF<sub>2</sub> results. As on-time is increased from 2 ms to 150 ms, the %CF<sub>2</sub> in the film decreased from 70% to 36%. Also, a 36 %CF<sub>2</sub> content at a duty cycle of 150/400 is comparable to the 39% at 10/20. Due to the longer on-time and possible net deposition occurring during the plasma, a greater overall fraction of the film may be exposed to the defluorinating plasma. Furthermore, greater fragmentation of gas-phase CF<sub>2</sub> (Eq. 2-4) may be occurring as on-time is increased. Both these effects may result in lowering the %CF<sub>2</sub> in the films.

#### H. Process Time

In Figure 11a, the overall deposition rate ( $\mu\text{m/hr}$ ) as a function of off-time is shown for data in Fig. 4a. At an off-time of 400 ms, the time to deposit 1  $\mu\text{m}$  would be 38 minutes while with a 30 ms off-time, it would take 10 minutes. Furthermore, the maximum overall deposition rate will occur with an off-time between 30 and 70 ms. In Figure 11b, deposition rate ( $\mu\text{m/hr}$ ) as a function of off-time is shown for data in Fig. 10a. As on-time is increased the overall deposition rate increases. For a pulse cycle of 150/400, a 1  $\mu\text{m}$  thick film would take 15 minutes. In comparison, even though the average input power for pulse cycles of 10/50 and 80/400 are the same, the overall deposition rate is higher for the pulse cycle of 10/50. Thus, the overall deposition rate is not solely a function of duty cycle, as shown by Fig 11c. This shows that gas-phase

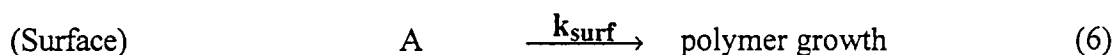
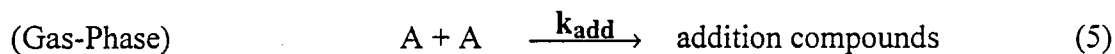
chemistry is important and differences in transient gas-phase concentrations must be responsible for these observations.

## IV. Reactor Deposition Model

### A. Derivation of Deposition Model

Pulsing the input power creates two distinct conditions, the presence of a glow discharge and its absence. The glow discharge present during the on-time contains electrons, ions, fluorine atoms, other neutrals, excited species and the original monomer. When the plasma is extinguished, extremely short lived species no longer contribute to the deposition of a plasma polymer. The short(<1 ms) lived species are electrons, ions,<sup>43</sup> and metastable fluorine atoms.<sup>44</sup> It is the long(> 10 ms) lived neutrals,  $CF_x$  ( $x = 1, 2, 3$ ) species, created in the plasma that are available for deposition.<sup>25, 45</sup> Thus, some of the complicated interactions that exist in plasmas are eliminated during the off-time. This simplifies modeling of the deposition behavior.

During the off-time, when glow discharge is absent, the polymerizing precursors,  $CF_x$  species (A), are lost through convection, homogeneous gas-phase recombination and heterogenous surface reactions. The rate of convective loss is related to the residence time,  $\tau$ , of the CVD reactor. Simplified mechanisms for loss through gas-phase and surface reactions are



where the gas-phase addition reaction does not lead to deposition while the surface reaction does.

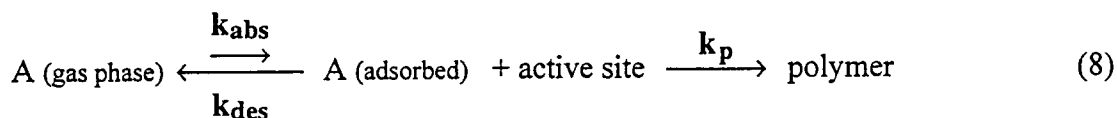
For gas-phase addition(Eq. 5), the rate,  $r_{add}$ , is assumed to be second order in A.

$$r_{add} = k_{add} [A] [A] \quad (7)$$

Although many gas phase addition reactions are possible, arising from the recombination of different species, only a single combined rate constant will be used.

This combined rate constant,  $k_{add}$ , will be compared to the second order reaction constant for two  $CF_2$  forming  $C_2F_4$ . The latter rate constant has been measured and was determined to be independent of pressure from 1.5 to 734 torr.<sup>46</sup> It is also assumed that the addition compounds from Eq. 5 do not contribute to polymer growth on the surface and are lost through the convective process.

Surface loss of  $CF_x$  which leads to polymer growth is expressed as a first order process. This originates from the most commonly proposed mechanism<sup>8</sup> for fluorocarbon polymer growth:



For film growth, A must adsorb onto the surface and afterwards polymerize with an active site ( $\theta^*$ ). The adsorption and desorption rate constants,  $k_{ads}$ , and  $k_{des}$  respectively depend on substrate temperature. The observed rate of film deposition has an apparent negative activation energy. In other words, the films grow more slowly at higher substrate temperatures. This is consistent with an adsorption limited process.<sup>41</sup> The

active sites which react with adsorbates can be free radicals, chain ruptures, or any point of polymer growth.<sup>8</sup> Assuming the adsorption and desorption steps are in equilibrium and can be described by a Langmuir isotherm at low fractional coverage, the process becomes an apparent first order reaction.<sup>47</sup> The first order kinetics for  $CF_x$  reactions on surfaces are consistent with several reported studies.<sup>25, 48</sup> These studies were carried out at low pressure (<500 mtorr), where gas-phase addition reactions are slow. The rate expression for polymer growth on the surface is

$$r_{\text{surf}} = k_{\text{surf}} [A] \quad (\text{mol/cm}^2 \text{ s}) \quad (9)$$

where  $k_{\text{surf}} = RT_g (k_{\text{abs}}/k_{\text{des}}) k_p [\theta^*]$ . The first order rate constant for heterogeneous surface reaction is  $k_{\text{surf}}$  (cm/s) where  $R$  is the universal gas constant,  $T_g$  is the gas temperature,  $k_{\text{abs}}/k_{\text{des}}$  is the ratio of the adsorption and desorption rate constants,  $k_p$  is the polymerization rate constant for adsorbed species, and  $[\theta^*]$  is the areal concentration of active sites.

In order to model film growth from  $CF_x$ , two cases will be examined. Case 1 will encompass all the mechanisms described for  $CF_x$  loss and Case 2 will be the limiting condition when gas-phase addition is not important. Figure 12 shows the relationship of the control volume for the mass balance on gas-phase  $CF_x$  to the CVD reactor geometry. This control volume spans in-between the electrodes with the radial distance being very

small in order to eliminate any radial concentration gradients. An overall gas-phase  $CF_x$  mass balance over the control volume yields

$$\frac{d[A]}{dt_{off}} = - \frac{S}{V_r} k_{surf} [A] - k_{add} [A] [A] - \frac{[A]}{\tau} \quad (\text{Case 1}) \quad (10)$$

$$\frac{d[A]}{dt_{off}} = - \frac{S}{V_r} k_{surf} [A] - \frac{[A]}{\tau} \quad (\text{Case 2}) \quad (11)$$

where  $[A]$  is the gas phase concentration of  $CF_x$  and  $S$  is the surface area of the electrodes in the control volume,  $V_r$ . For our parallel plate geometry (Fig. 1), the ratio  $S/V_r$  simplifies to  $2/h$  where  $h$  is the electrode spacing.

Integrating the overall mass balances (Eqs. 10 and 11) yields the expressions for the concentration of  $CF_x$  in the gas phase during the off-time.

$$[A] = \frac{[A]_o \exp\left[-\left(\frac{S}{V_r} k_{surf} + \frac{1}{\tau}\right) t_{off}\right]}{1 + \frac{[A]_o k_{add}}{\frac{S}{V_r} k_{surf} + \frac{1}{\tau}} \left\{1 - \exp\left[-\left(\frac{S}{V_r} k_{surf} + \frac{1}{\tau}\right) t_{off}\right]\right\}} \quad (12)$$

(Case 1)

$$[A] = [A]_o \exp\left[-\left(\frac{S}{V_r} k_{surf} + \frac{1}{\tau}\right) t_{off}\right] \quad (\text{Case 2}) \quad (13)$$

In these expressions, the initial gas phase concentration of  $CF_x$  at the end of the on-time and at the beginning of the off-time is defined as  $[A]_o$ . The initial concentration,  $[A]_o$ ,

will be a function of all the parameters that are involved in creating  $CF_x$  species from the monomer. These parameters are on-time, duty cycle, pressure and input power.

Integrating the rate of polymer growth (Eq. 9) from 0 ms to  $t_{off}$  using Eqs. 12 and 13 gives

$$G_{off} = \frac{B k_{surf}}{k_{add}} \ln \left\{ 1 + \frac{[A]_0 k_{add}}{\frac{S}{V_r} k_{surf} + \frac{1}{\tau}} \left[ 1 - \exp\left[-\left(\frac{S}{V_r} k_{surf} + \frac{1}{\tau}\right) t_{off}\right] \right] \right\} \quad (\text{Case 1}) \quad (14)$$

$$G_{off} = \frac{[A]_0 B k_{surf}}{\frac{S}{V_r} k_{surf} + \frac{1}{\tau}} \left[ 1 - \exp\left[-\left(\frac{S}{V_r} k_{surf} + \frac{1}{\tau}\right) t_{off}\right] \right] \quad (\text{Case 2}) \quad (15)$$

where  $G_{off}$  is the growth during each cycle and  $B$  is the inverse molar density for bulk PTFE. Using a density of  $2.2 \text{ g/cm}^3$  and molecular weight of  $50 \text{ g}$  for a  $CF_x$  unit, the constant  $B$  is calculated to be  $2.27 \times 10^9 \text{ Å cm}^2/\text{mole}$ . The constant,  $B$ , is a proportionality constant that changes the areal deposition amount to a thickness amount. Thus,  $G_{off}$  is the thickness that has deposited during the off-time,  $t_{off}$ , and has units of  $\text{Å}$ .

Furthermore, since either net etching or net growth can occur during the on-time, the measured growth,  $G_{meas}$ , is equated to the sum of the growth during the off-time,  $G_{off}$ , and the net thickness change during the on-time,  $G_{on}$ .

$$G_{meas} = G_{off} + G_{on} \quad (16)$$

Equation 16 allows a least squares non-linear regression of the experimentally measured growth. The adjustable parameters for the fits were  $k_{\text{surf}}$ ,  $k_{\text{add}}$ ,  $[A]_0$ , and  $G_{\text{on}}$ . For these regressions all the data were weighted equally. The results of the regression shown will be described by either a solid or dashed line.

## B. Spatial Concentration Uniformity

As the model is based upon the control volume being well-mixed, that is, it behaves as a continuously stirred tank reactor (CSTR), the validity of the CSTR condition needs to be examined. The CSTR model requires that negligible concentration gradients must exist in the gas-phase.

The dimensionless Peclet number,  $Pe$ , is the ratio of convective transport to diffusive transport and is defined by

$$Pe = \frac{v}{D/L} \quad (17)$$

where  $v$  equals the bulk gas velocity,  $D$  is the mass diffusivity, and  $L$  is the characteristic length in this reactor. For  $Pe \rightarrow 0$ , the system is well-mixed and can be modeled after a CSTR. For  $Pe \rightarrow \infty$ , the system becomes a plugged flow reactor(PFR).<sup>47</sup>

For fast surface reactions, the evaluation of mass transport limitation due to surface reactions can be characterized with the dimensionless Damkohler number,  $Da_s$ . The Damkohler number is the ratio of the reaction velocity at a surface to the diffusion velocity to that surface and is defined by

$$Da_s = \frac{k_{surf}}{D/L} \quad (18)$$

where  $k_{surf}$  is the first order reaction rate constant for the heterogeneous surface reaction as shown in Eq. 9. For  $Da_s \rightarrow 0$ , the system is well-mixed and for  $Da_s \rightarrow \infty$ , significant axial gradients develop as a result of reactant depletion at the growth surface.<sup>42, 48</sup>

The mass diffusivity of  $CF_2$  was estimated using the method of Hirshfield et. al.<sup>49</sup> with estimates of Lennard-Jones potentials taken from the work of Selva.<sup>50</sup> This gave a value of  $43 \text{ cm}^2/\text{s}$  at 1000 mtorr and was used as the average value of  $D$  for  $CF_x$ . Note that the calculated  $D$  for  $CF$  and  $CF_3$  are 57 and  $36 \text{ cm}^2/\text{s}$  respectively at 1000 mtorr. With the flow rate at 23 sccm and pressure at 1000 mtorr, the axial Pe number for  $CF_2$  was calculated to be 0.04 and the surface Damkohler number for  $CF_2$  was found to be 0.45. For the latter calculation a value of  $k_{surf} = 15.2 \text{ cm/s}$  used. The origin of this value will be describe later in this work. Because both the  $Da_s$  and Pe numbers are less than 1, the assumption of negligible axial concentration gradients between the electrodes is reasonable.

## V. Comparison of Data with Deposition Model

### A. Analysis of $k_{\text{surf}}$ , $k_{\text{add}}$ , $[A]_0$ , and $G_{\text{on}}$

The model was applied to three sets of data. The first set of off-time deposition data had the same input power, on-time, and substrate temperature while differing in flow rate, pressure, and electrode spacing. It consisted of the 1200, 1000, 750, and 400 mtorr runs at 23 sccm, the 1000 mtorr runs at 12.5 and 5.1 sccm, and the 1000 mtorr run at 1/2 inch electrode spacing. From this first set, the parameters  $k_{\text{surf}}$ ,  $k_{\text{add}}$ , and  $[A]_0$  were determined and applied to the second and third sets of data. The second set of data contains deposition data from changing the substrate temperature. The third set contains deposition data from varying on-time with a constant off-time.

Because the first set of data had the same input power, substrate temperature, and short on-time, the parameters  $k_{\text{surf}}$ ,  $[A]_0$ , and  $G_{\text{on}}$  were either considered constant or related to pressure and flow rate. The surface rate constant would be most affected by substrate temperature changes and thus was assumed to be constant for the first data set. For  $[A]_0$ , the experimental data in Fig. 5b shows  $G_{\text{meas}}$  having a linear relationship with pressure which may result from gas-phase concentration of  $\text{CF}_x$  being proportional to pressure. Since HFPO has been found to thermally decompose with first order kinetics to form  $\text{CF}_2$ ,<sup>35</sup> the most likely mechanism for the decomposition of HFPO in the plasma is:



The plasma decomposed  $\text{CF}_2$  radical is assumed to be the starting point for all  $\text{CF}_x$  species in the gas phase. In Equation 26, assuming the plasma electron density does not change much with pressure and conversion of HFPO is small during the 10 ms on-period, the loss due to convection, the surface reaction, and homogenous reaction can be neglected to yield a first order reaction in HFPO. When conversion is small, the concentration of HFPO will not change much and the initial  $\text{CF}_x$  concentration will be proportional to pressure resulting in

$$[A]_0 = k_{\text{hfpo}} (P / RT_g) t_{\text{on}} \quad (20)$$

where  $t_{\text{on}}$  is the on-time and  $k_{\text{hfpo}}$  is equal to the product of the plasma electron density and  $k_e$  in Eq. 19.

During the on-time, etching from fluorine atoms and ion bombardment competes with deposition from  $\text{CF}_x$  species and can result in a negative  $G_{\text{on}}$  value (net etching of the film). Flow rate and pressure influences the energy and flux of ion bombardment. As pressure increases, mean free path decreases, which decreases the average energy of the bombarding ions, decreasing the etching rate. As the flow rate increases, the overall energy input per molecule decreases, also decreasing the etch rate. Thus, for fixed on-time, the parameter  $G_{\text{on}}$  will be simplified and assumed to be

$$G_{\text{on}} = g_{\text{on}} (1 / P Q) \quad (21)$$

where  $P$  is the pressure,  $Q$  is the flow rate in sccm, and  $g_{\text{on}}$  is a negative proportionality constant. As for the parameter  $k_{\text{add}}$ , it is assumed to be constant for all data sets since the fluorine to carbon ratio for  $\text{CF}_x$  species were relatively similar.

Nonlinear least squares regression of Case 1 and 2 to the first data set was performed. Case 1 had 4 parameters ( $[A]_0/P$ ,  $k_{\text{surf}}$ ,  $g_{\text{on}}$ , and  $k_{\text{add}}$ ) and Case 2 had 3 parameters ( $[A]_0/P$ ,  $k_{\text{surf}}$ , and  $g_{\text{on}}$ ). The total number of experimental data points used was 66. Using the least-squares fit parameters (Table II), model predictions versus the experimentally measured data are shown for Case 1 (Fig. 13a) and Case 2 (Fig. 13b). The solid line is for the condition when the model value equals the experimental. Both models correlate well as shown by the corresponding coefficient of determination ( $R^2$ ) and chi square ( $\chi^2$ ) values.

Statistically, Case 1 provides a better description of the data because it has a higher  $R^2$  and lower  $\chi^2$  than Case 2. Chi square ( $\chi^2$ ) is the sum of the squared difference between the model and experiment. Using chi square values in a F-test,<sup>51</sup> at the 95% confidence level Case 1 is to be preferred and the hypothesis that gas-phase addition reactions is significant is confirmed. Thus,  $[A]_0/P$  is higher and  $k_{\text{surf}}$  is lower for Case 1 than for Case 2 because loss by gas-phase addition is being accounted for by Case 1. Also, the gas-phase addition rate constant,  $k_{\text{add}}$ , of  $1.0 \times 10^{10} \text{ cm}^3/\text{s mol}$  is comparable to the experimental values of second order rate constants for two reacting  $\text{CF}_2$  to form  $\text{C}_2\text{F}_4$ . At 300 K, the experiment rate constants are  $1.2$  to  $2.4 \times 10^{10} \text{ cm}^3/\text{s mol}$ <sup>52</sup> and  $3$  to  $6.3 \times 10^{10} \text{ cm}^3/\text{s mol}$ <sup>46</sup> respectively. For all further analysis only Case 1 parameters and fits will be discussed.

The earlier assumption that  $[A]_0$  is proportional to pressure,  $k_{\text{surf}}$  is constant, and  $G_{\text{on}}$  is inversely proportional to pressure and flow rate resulted in good correlation

between the model and the experimental data. The value of  $1.04 \times 10^{-9}$  moles / cm<sup>3</sup> torr for  $[A]_0/P$  corresponds to a 2% HFPO conversion to CF<sub>x</sub>. Thus the concentration of CF<sub>x</sub> during the on-time will be small. In addition, a constant  $k_{\text{surf}}$  may indicate that active site concentrations are not sensitive to flow rate, pressure, and electrode spacing changes.

Using the first order surface rate constant, an apparent sticking CF<sub>x</sub> coefficient is described by

$$\gamma = \frac{4 k_{\text{surf}}}{\bar{c}} \quad (22)$$

where  $\bar{c}$  is the mean molecular velocity.<sup>53</sup> Eq. 22 is the ratio of the surface reaction rate(Eq. 9) to the CF<sub>x</sub> flux. This flux is defined by

$$\text{flux}_{\text{CF}_x} = \frac{[A] \bar{c}}{4} \quad (23)$$

Using  $k_{\text{surf}} = 15.2$  cm/s and calculating the mean CF<sub>2</sub> velocity to be  $3.56 \times 10^4$  cm/s at 300 K, the calculated apparent sticking coefficient onto a fluorocarbon surface is  $1.7 \times 10^{-3}$ . This value is similar to the apparent sticking coefficient of  $10^{-3}$  to  $10^{-4}$  found by Gray et. al.<sup>54</sup> using molecular beam studies of HFPO. On the other hand, this value is low compared to the apparent sticking coefficients(  $\sim 10^{-1}$  to  $10^{-2}$ ) for CF<sub>2</sub> onto bare metal oxide surfaces.<sup>25</sup> It may be that CF<sub>x</sub> species absorb less readily on fluorocarbon surfaces than on metal oxide surfaces. Indeed, a decrease in the CF<sub>2</sub> loss rate has been observed when the reactor surface was covered with a fluorocarbon layer.<sup>45, 55</sup>

Lastly, the  $G_{\text{on}} * P * Q$  value of -3.45 Å/torr-sccm indicates that depending on pressure and flow rate slow etching may be occurring during the 10 ms on-time. At 1000

mtorr and 23 sccm,  $G_{on}$  will be  $-0.15 \text{ \AA}$  amounting to less than 10% of the maximum deposition possible ( $1.8 \text{ \AA}$ ). Furthermore, negative values for  $G_{on}$  are consistent with net etching at short on-times and small  $CF_x$  concentrations.

Using the least-square fit parameter for Case 1 (Table 2), the model prediction is plotted for different pressures, flow rates, and electrode spacing data as a function of off-time. In Figure 5a, good agreement of the model is obtained at 1200, 1000, and 750 mtorr. The correlation is not so good for the 400 mtorr (Fig. 5a). As pressure is increased,  $[A]_0$  increases proportionally which accounts for the higher maximum deposition per cycle. Figure 6 shows the model describes the results at different flow rates. Little change is seen between the 12.5 sccm and 23 sccm model predictions because the effect of residence time is small compared to the first order surface rate constant. On the other hand, the model at 5.1 sccm predicts a lower maximum deposition per cycle because more etching is occurring during the on-time. Because the molecules stay in the reactor longer, greater defragmentation occurs which leads to greater etching. Lastly, in Figure 9, with the electrode spacing at 1/2 inch, the model was able to describe the data well. Because the volume was halved, the model predicted a maximum deposition which was about half that of the 1" electrode spacing volume. This further confirms that the plasma concentration may not have changed much when the electrode spacing was reduced.

#### **B. Applications for the Model Parameters $k_{surf}$ , $k_{add}$ , and $[A]_0$ .**

The second set of data were all deposited at 1000 mtorr, 12.5 sccm, and 280 watts peak input power. Only the substrate temperature was varied. An Arrhenius expression

for the surface rate constant,  $k_{surf}$ , allows non-linear regression of the model(Eq. 14 and 16) against the experimental deposition data at various substrate temperatures using the Case 1 parameter values for  $[A]_0$ ,  $k_{add}$ , and  $G_{on}$  found in Table 2.

From the deposition rate equation (Eq. 9),  $k_{surf}$  is proportional to  $(k_{abs}/k_{des}) k_p$ . The combined Arrhenius rate expression is

$$k_{surf} = k_0 \exp [ - (\Delta H_{ads} + E_a)/RT_s ] \quad (24)$$

where the Arrhenius rate constant for  $k_{surf}$  is composed of the pre-exponential factor,  $k_0$ , and the combined apparent activation energy ,  $\Delta H_{ads} + E_a$ . The heat of adsorption,  $\Delta H_{ads}$ , is derived from the rate constant ratio,  $k_{ads}/k_{des}$  , while  $E_a$  is the activation energy for the radical, A, and active site reaction.

A non-linear least square fit with  $k_0$  and  $(\Delta H_{ads} + E_a)/R$  as the adjustable parameters was performed unto temperature substrate data at 10 ms on-time and 400 ms off-time(Fig. 7a). Furthermore, the upper electrode was assumed to be at room temperature while the lower electrode was at the specified temperature. Because mass transport limitations may be occurring at low substrate temperatures due to high deposition rates, only the experimental data points above room temperature were used for the regression and are marked with an open box symbol. Thus, the model fits the data well for data above room temperature with  $R^2 = 0.994$  but it deviates at the lower temperatures. This deviation is consistent with the possibility of mass transport limitations at higher deposition rates.

The least square fit resulted in  $k_0 = (5.90 \pm 0.97) \times 10^{-2}$  cm/s and a negative value of  $-3.29 \pm 0.11$  kcal / mole for  $\Delta H_{ads} + E_a$ . Assuming the absolute value of  $\Delta H_{ads}$  is much

greater than  $E_a$ , the low apparent activation energy is comparable to the activation energy for physisorption which is typically around -5 kcal/mole.<sup>47</sup> In comparison, activation energies for chemisorption processes are around -50 kcal/mole.<sup>47</sup> Using the Arrhenius parameters,  $k_{surf}$  at -35 °C is estimated to be 60 cm/s which translates to a  $Da_s$  of 1.7. A  $Da_s$  greater than one provides more support for mass transport limitations existing at lower substrate temperatures. Furthermore, at  $T_s = 20$  °C,  $k_{surf}$  is calculated to be 16.3 cm/s by Eq. 24 which is consistent with the best fit room temperature result of 15.2 cm/s in Table 2.

The validity of the Arrhenius parameters can be tested by comparing the model to substrate temperature data at 70 °C (Fig 8). Using the Arrhenius model, at 70 °C,  $k_{surf}$  is calculated to be 7.2 cm/s by Eq. 24 with a margin of error of  $\pm 1.4$  cm/s. The parameter values used were Table 2 values for  $[A]_0$ ,  $k_{add}$ , and  $g_{on}$ . The model was able to predict the experimental deposition data at 70° C.

### C. On-Time Analysis Using Model Parameters

When the plasma is present, both deposition from  $CF_x$  species and etching from ion bombardment and fluorine will occur. The corresponding net etch/growth rate during the on-time is

$$\frac{d G_{on}}{d t_{on}} = B k_{surf} [A] - E_s \quad (25)$$

where  $[A]$ , the concentration of  $CF_x$ , will vary during the on-time. The etching rate,  $E_s$ , will be assumed to be constant. In support of this assumption, ion bombardment is expected to be the major mechanism for etching, the concentration of ions and electrons

will reach steady state within several hundred microseconds.<sup>43</sup> This time scale is short compared to the typical 10 ms on-time. During the majority of the on period, the constant flux will correspond to a constant ion induced etching rate.

During the on-time, [A] will depend on the decomposition of HFPO(Eq. 19), surface loss, gas-phase loss, and convective loss. It is assumed that any CF<sub>x</sub> production from surface etching is negligible. Thus, the overall gas-phase CF<sub>x</sub> and HFPO mass balances over the control volume are

$$\frac{d[A]}{dt_{on}} = k_{hfpo} [HFPO] - \frac{S}{V_r} k_{surf} [A] - k_{add} [A] [A] - \frac{[A]}{\tau} \quad (26)$$

$$\frac{d[HFPO]}{dt_{on}} = - k_{hfpo} [HFPO] + \frac{[HFPO]_0 - [HFPO]}{\tau} \quad (27)$$

Using Equations 25 - 27, [A] and G<sub>on</sub> can be solved as a function of on-time. The parameter values in Table 2 were used for [A]<sub>0</sub>, k<sub>add</sub>, and k<sub>surf</sub>. The [A]<sub>0</sub> value of 1.04 x 10<sup>-9</sup> moles/cm<sup>3</sup> at 10 ms was used to determine a k<sub>hfpo</sub> value of 2.2 cm<sup>3</sup>/s mol(Eq. 19). It was assumed that at 10 ms, the rate of production of [A] was much greater than the loss rates(Eq. 26). Furthermore, [HFPO]<sub>0</sub> is 5.35 x 10<sup>-8</sup> moles/cm<sup>3</sup> and τ is 1500 ms for conditions at 1000 mtorr and 12.5 sccm.

Figure 14, [A] is plotted as a function of on-time. There is a maximum at 70 ms which corresponds to [A] = 2.6 x 10<sup>-9</sup> moles/cm<sup>3</sup>. A steady state value of 1.14 x 10<sup>-9</sup>

moles/cm<sup>3</sup> is reached after two seconds which is representative of a continuous run condition. At 10 ms, a concentration of  $1.04 \times 10^{-9}$  moles/cm<sup>3</sup> is predicted.

The temporal variation in [A] can be used to predict  $G_{on}$ , the thickness deposited(or lost) during the on-time, for different etching rates,  $E_s$ , as shown in Fig. 15a and 15b. Using Eq. 25 and the steady state [A] value,  $E_s$  at 0.0392 Å/ms will result in no addition change in  $G_{on}$  at long on-times. Also, an  $E_s$  value of 0.057 Å/ms will result in a net etch. In Fig 15a, the respective growth and etch rates are seen in the slopes at steady state conditions (>2 sec). With longer on-times, the model predicts either larger etched( $E_s > 0.0392$ ) or deposited( $E_s < 0.0392$ ) amounts. In Figure 15b, for  $E_s$  values of 0.0392 and 0.057 Å/ms a net etch is predicted for on-times less than 20 and 40 ms respectively. This is due to low [A]. This observation is consistent with the assumption that at 10 ms on-time a net etch will occur.

With predicted  $G_{on}$  and  $G_{off}$  values, the model can be compared to deposition per cycle data for different on-time times while keeping off-time constant at 400 ms(Fig. 10a). It is assumed that a 400 ms off-time is sufficiently long to deplete nearly all of the gas-phase  $CF_x$  species before the next rf pulse. To support this assumption, the expression for  $CF_x$  concentration during the off-time(Eq. 12) using a maximum possible initial  $CF_x$  concentration of  $2.6 \times 10^{-9}$  moles/cm<sup>3</sup>, shows that 99.8% of  $CF_x$  gas-phase species are depleted. In Figure 16, model prediction of total deposition per cycle is in comparison with experimental deposition per cycle data. The parameter  $E_s$  was adjusted to provide the best fit possible. The predicted values with  $E_s$  between 0.061 Å/ms and 0.057 Å/ms

correlate well with the experiment data. Furthermore, the model is sensitive to  $E_s$  changes at longer on-times as  $E_s$  values of 0.050 and 0.070 Å/ms did not correlate well.

#### **D. Sensitivity Analysis**

The sensitivity of the predicted data to parameter changes for  $[A]_0$ ,  $k_{surf}$ ,  $k_{add}$ , and  $G_{on}$ , is listed in Table 3. Case 1 is used and each parameter is varied by 10% with the central values from Table 2. In Table 3, the % deviation from the central values are listed for each parameter changed. For changes in  $[A]_0$ ,  $k_{surf}$ , and  $g_{on}$ , the predicted deposition data is more sensitive at the lower off-times as the % deviation decreases as off-time is increased. On the other hand, changes in  $k_{add}$  results in the model being more sensitive at longer off-times. At the maximum deposition region (>400 ms off-time), the model is most sensitive to changes in  $[A]_0$ , while least sensitive to changes in  $g_{on}$ .

## VI. Conclusions

Pulsed plasma deposition can be used to molecularly tailor the composition of CVD fluorocarbon films and deposition rates. Keeping all other parameters fixed, films deposited from a pulsed plasma had significantly higher  $\text{CF}_2$  fractions than films from a continuous plasma. Since pulsing the plasma excitation varies the degree of ion bombardment and chemical etching of the growing surface, it may limit defluorination reactions caused by ion bombardment and chemical etching. Comparison of deposition onto grounded and electrically isolated substrates showed that ion bombardment is not a major factor in determining film composition at low pulse cycles. In addition, duty cycle alone does not determine deposition rate. Even though the average power for 10/50 and 80/400 pulse cycles is the same, different deposition rates were measured. Differences in transient gas phase concentrations must be responsible for these observations. While the importance of duty cycle had been previously appreciated,<sup>34</sup> the experiments in this work highlight the additional importance of overall cycle time as compared to the transient build-up and decay of gaseous species in the CVD reactor.

Plasma chemistry can be very complex which makes it difficult to control selectivity. Since HFPO has a known gas-phase decomposition pathway to difluorocarbene, pulsed excitation may provide a way to favor this reaction pathway over the formation of other decomposition products. Indeed, short on-times resulted in the highest  $\%\text{CF}_2$  in the film. In addition, shorter off-times lowered the  $\%\text{CF}_2$  in the film. Thus, subjecting reactant molecules to multiple rf pulse may enhance undesirable

fragmentation reactions. In order to deposit films with a high %CF<sub>2</sub>, we speculate that pulse conditions must be selected which result in both a high gas-phase mole fraction of difluorocarbene relative to other film forming fluorocarbon species such as CF<sub>3</sub> and CF. In addition, once the CF<sub>2</sub> polymerizes on the surface, it must be protected from surface defluorination reactions. This can be achieved by maintaining low duty cycles.

Generally, the deposition per cycle as a function of off-time increased monotonically until a plateau region was reached. The deposition per cycle ( $G_{\text{on}} + G_{\text{off}}$ ) increased with increasing pressure, flow rate, electrode spacing, off-time, on-time, and decreasing substrate temperature. As for the total process deposition rate [ $(G_{\text{on}} + G_{\text{off}})/(t_{\text{on}} + t_{\text{off}})$ ], it increased with the same conditions except for decreasing off-time.

A simplified model of the thickness deposited during each cycle was developed. During the off-period, the model accounts for loss of film precursor by convection and second order homogeneous recombination in addition to consumption by first order film growth. During the on-period, a single set of parameters were found that describe the growth rate under a variety of different conditions. Previous modeling of pulsed plasma chemistry neglected gas-phase recombination reactions. Here, the effect of homogeneous recombination was found to be significant statistically. In addition, the model in this paper is compared to a wide range of experimental measurements. The general features of the model are common to many plasma deposition processes. Thus, the model may be applicable to pulsed PECVD from other precursor gases.

## VII. Acknowledgements

We wish to gratefully acknowledge the NIH for support of this work under contract NO1-NS-3-2301.

## VIII. References

- (1) Ratner, B. D.;Chilkoti, A.; Lopez, G. P., "Plasma Deposition and Treatment for Biomaterial Applications" in *Plasma Deposition, Treatment, and Etching of Polymers*;Academic Press: San Diego, 1990.
- (2) Ehrlich, P., *J. Res. Natl. Std.* **1953**, *51*, 185.
- (3) Gangal, S. V., "Tetrafluoroethylene Polymers" in *Encyclopedia of Polymer Science and Engineering*;John Wiley and Sons, Inc.: 1989.
- (4) Thomson, L. A.;Law, F. C.;James, K. H.; Rushton, N., *Biomaterials* **1991**, *12*, 781.
- (5) Guidoin, R.;Chakfe, N.;Maurel, S.;How, T.;Batt, M.;Marois, M.; Gosselin, C., *Biomaterials* **1993**, *14*, 678.
- (6) Ocumpaugh, D. E.; Lee, H. L., "Foreign Body Reactions to Plastic Implants" in *Biomedical Polymers*;Marcel Dekker, Inc.: New York, 1971.
- (7) Yasuda, H., *Plasma Polymerization*; Academic Press: Orlando, 1985.
- (8) d'Agostino, R.;Cramarossa, F.;Fracassis, F.; Illuzzi, F., "Plasma Polymerization of Fluorocarbons" in *Plasma Deposition Treatment, and Etching of Polymers*;Academic Press: San Diego, 1990.
- (9) Bell, A. T., *Top. Curr. Chem.* **1980**, *94*, 43.
- (10) Kay, E.;Coburn, J.; Dilks, A., *Top. Curr. Chem.* **1980**, *94*, 1.
- (11) Dilks, A.; Kays, E., *Macromolecules* **1981**, *14*, 855.
- (12) Iriyama, Y.; Yasuda, H., *J. Polym. Sci., Part A: Polym. Chem.* **1992**, *30*, 1731.

- (13) Nakajima, K.; Bell, A. T.; Shen, M.; Millard, M. M., *J. Appl. Polym. Sci.* 1979, 23, 2627.
- (14) Morosoff, N.; Yasuda, H.; Brandt, E. S.; Reilley, C. N., *J. Appl. Polym. Sci.* 1979, 23,
- (15) Yasuda, H.; Wang, C. R., *J. Polym. Sci.: Polym. Chem. Ed.* 1985, 23, 87.
- (16) Limb, S. J.; Gleason, K. K.; Edell, D. J.; Gleason, E. F., *J. Vac. Sci. Technol.* 1997, A15, To be published in August.
- (17) Gambogi, R. J.; Cho, D. L.; Yasuda, H.; Blum, F. D., *J. Polym. Sci., Part A: Polym. Chem.* 1991, 29, 1801.
- (18) Sugimoto, I., *Macromolecules* 1991, 24, 1480.
- (19) O'Kane, D. F.; Rice, D. W., *J. Macromol. Sci.-Chem.* 1976, A10, 567.
- (20) Yasuda, H., *J. Polym. Sci., Macromol. Rev.* 1981, 16, 199.
- (21) d'Agostino, R.; Cramorossa, F.; Fracassi, F.; Desimoni, E.; Sabbatini, L.; Zambonin, P. G.; Caporiccio, G., *Thin Solid Films* 1986, 143, 163.
- (22) d'Agostino, R.; Favia, P.; Fracassi, F.; Illuzzi, F., *J. Polym. Sci., Part A: Polym. Chem.* 1990, 28, 3387.
- (23) Savage, C. R.; Timmons, R. B.; Lin, J. W., *Adv. Chem. Ser.* 1993, 236, 745.
- (24) Yasuda, H.; Hsu, T., *J. Polym. Sci.: Polym. Chem. Ed.* 1977, 15, 81.
- (25) Booth, J. P.; Hancock, G.; Perry, N. D.; Toogood, M. J., *J. Appl. Phys.* 1989, 66, 5251.
- (26) Richard, P. D.; Mackunas, R. J.; Lucovsky, G.; Fountain, G. G.; Mansow, A. N.; Tsu, D. V., *J. Vac. Sci. Technol.* 1985, A3, 867.

- (27) Savage, C. R.; Timmons, R. B.; Lin, J. W., *Chem. Mater.* **1991**, *3*, 575.
- (28) Jiang, P.; Economou, D. J.; Shin, C. B., *Plasma Chem. and Plasma Process.* **1995**, *15*, 383.
- (29) Samukawa, S., *Applied Physics Letter* **1994**, *64*, 3398.
- (30) Mackie, N. M.; Dalleska, N. F.; Castner, D. G.; Fisher, E. R., *Chem. Mater.* **1997**, *9*, 349.
- (31) Mantzaris, N. V.; Boudouvis, A.; Gogolides, E., *J. Appl. Phys.* **1995**, *77*, 6169.
- (32) Gogolides, E.; Stathakopoulos, M.; Boudouvis, A., *J. Phys. D: Appl. Phys.* **1994**, *27*, 1878.
- (33) Bariya, A. J.; Frank, C. W.; McVittie, J. P., *J. Electrochem. Soc.* **1990**, *137*, 2575.
- (34) Park, S. K.; Economou, D. J., *J. Electrochem. Soc.* **1990**, *137*, 2103.
- (35) Knickelbein, M. B.; Webb, D. A.; Grant, E. R., *Mat. Res. Soc. Symp. Proc.* **1985**, *38*, 23.
- (36) Limb, S. J.; Labelle, C. B.; Gleason, K. K.; Edell, D. J.; Gleason, E. F., *Appl. Phys. Lett.* **1996**, *68*, 2810.
- (37) Wells, R. K.; Ryan, M. E.; Badyal, J. P. S., *J. Phys. Chem.* **1993**, *97*, 12879.
- (38) Wheeler, D. R.; Pepper, S. V., *J. Vac. Sci. Technol.* **1982**, *20*, 226.
- (39) Clark, D. T.; Brennan, W. J., *J. of Elect. Spect. and Rel. Phenon* **1986**, *41*, 399.
- (40) d'Agostino, R.; Cramarossa, F.; Illuzzi, F., *J. Appl. Phys.* **1987**, *61*, 2754.
- (41) Laidler, K. J., *Fundamental Principles, Part I*; Reinhold: New York, 1984.

- (42) Fogler, H. S., *Elements of Chemical Reaction Engineering*; Prentice Hall PTR: Upper Saddle River, 1992.
- (43) Kono, A.; Haverlag, M.; Kroesen, G. M. W.; Hoog, F. J. d., *J. Appl. Phys.* 1991, 70, 2939.
- (44) Hansen, S. G.; Luckman, G.; Colson, S. D., *Appl. Phys. Lett.* 1988, 53, 1588.
- (45) Haverlag, M.; Stoffels, W. W.; Stoffels, E.; Kroesen, G. M. W.; Hoog, F. J. d., *J. Vac. Sci. Technol.* 1996, A14, 384.
- (46) Tyerman, W. J. R., *Transactions of the Faraday Society* 1969, 65, 1188.
- (47) Hill, C. G., *An Introduction to Chemical Engineering Kinetics and Reactor Design*; John Wiley & Sons: New York, 1977.
- (48) Kiss, L. D. B.; Sawin, H. H., *Plasma Chem. and Plasma Process.* 1992, 12, 523.
- (49) Reid, R. C.; Prausnitz, J. M.; Sherwood, T. K., *The Properties of Gases and Liquids*; McGraw-Hill: New York, 1977.
- (50) Svehla, R. A. *NASA Technical Report R-132*; NASA: Cleveland. 1962.
- (51) Shoemaker, D. P.; Garland, C. W.; Steinfeld, J. I.; Nibler, J. W., *Experiments in Physical Chemistry*; McGraw-Hill: New York, 1981.
- (52) Dalby, F. W., *J. Chem. Phys.* 1964, 41, 2297.
- (53) Chapman, B., *Glow Discharge Processes*; John Wiley & Sons: New York, 1980.
- (54) Gray, D. C., Thesis, Massachusetts Institute of Technology, 1992.
- (55) Booth, J. P.; Hancock, G.; Perry, N. D.; Blaikley, D. C. W.; Cairns, J. A.; Smailes, R., *Mat. Res. Soc. Symp. Proc.* 1987, 98, 135.

## Tables

**Table 1. Standard Process Conditions**

<b>Process Conditions</b>	<b>Set Point</b>
<b>Flow Rate</b>	<b>23 sccm</b>
<b>Pressure</b>	<b>1000 mtorr</b>
<b>Substrate Temperature</b>	<b>23 °C</b>
<b>On-time</b>	<b>10 ms</b>
<b>Off-time</b>	<b>400 ms</b>
<b>Peak rf Power</b>	<b>280 W</b>
<b>Substrate Potential</b>	<b>Electrically Grounded</b>

**Table 2. Best fit parameters for Case 1 and Case 2 deposition models**

	Case 1	Case 2
$R^2$	0.976	.969
$\chi^2$	0.611	0.833
$k_{\text{add}}$ $10^{10} \text{ cm}^3/\text{s mol}$	1.0	0.0
$[A]_0/P$ $10^{-9} \text{ moles/cm}^3 \text{ torr}$	1.04	0.738
$k_{\text{surf}}$ $\text{cm} / \text{s}$	15.2	18.3
$g_{\text{on}}$ $\text{\AA torr sccm}$	-3.45	-2.90

**Table 3. % Deviation from the central deposition per cycle value with a  $\pm 10\%$  change in a parameter.**

Off-time	Central Value	% Deviation in Deposition per Cycle with Each Parameter Change			
ms	Å/cycle	parameter varied			
		$[A]_o$	$k_{surf}$	$k_{add}$	$g_{on}$
10	0.47	$\pm 18$	$\pm 18$	$\pm 1$	$\pm 9$
50	1.26	$\pm 10$	$\pm 10$	$\pm 2$	$\pm 2$
100	1.72	$\pm 9$	$\pm 7$	$\pm 3$	$\pm 1$
200	2.05	$\pm 8$	$\pm 5$	$\pm 3$	$\pm 1$
400	2.15	$\pm 8$	$\pm 4$	$\pm 3$	$\pm 1$

## Figure Captions

Figure 1. a. Schematic diagram of the pulsed PECVD reactor. Cross-sectional view.

b. Resistively heated plate. The plate is electrically grounded and positioned on the lower electrode of the reactor.

Figure 2. C1s XPS of Pulsed and Continuous PECVD at 12.5 sccm, 1000 mtorr, and grounded substrate. a. Continuous, 50 watts. b. 10/400, 280 watts.

Figure 3. C1s XPS of pulsed and continuous PECVD at 12.5 sccm, 1000 mtorr, and electrically isolated substrate. a. Continuous, 50 watts. b. 10/400, 280 watts.

Figure 4. Deposition and composition changes as a function of off-time at 1000 mtorr and 23 sccm. a. Deposition per cycle. b.  $\text{CF}_2$  composition. All data were at a peak power of 280 W except for the open circle in b., which corresponds to 50 W.

Figure 5. a. Deposition per cycle as a function of off-time at 1200, 1000, 750, and 400 mtorr. The flow rate was 23 sccm. Case 1 model predictions are shown in comparison with experimental data. Parameter values in Table 2 were used. b. Deposition per cycle versus pressure for fixed off-times of 400 (filled circle) and 20 ms (open box).

Figure 6. Deposition per cycle versus off-time for three flow rates at 23, 12.5, and 5.1 sccm. Case 1 model predictions are shown in comparison with experimental data. Parameter values in Table 2 were used.

Figure 7. Substrate temperature effects on deposition per cycle and film composition. Deposited at 10/400 and 1000 mtorr with open symbols at 23 sccm and filled symbols at 12.5 sccm. a. Deposition per cycle data and non-linear least square fit of data for various substrate temperatures. b. Arrhenius plot

Figure 8. Deposition per cycle data versus off-time at 70 °C substrate temperature.

Figure 9. Deposition per cycle data as a function of electrode spacing. All data were deposited at 1000 mtorr. Case 1 model predictions are shown in comparison with experimental data. Parameter values in Table 2 were used.

Figure 10. Deposition per cycle data and film composition changes as a function of on-time. All films were deposited at 1000 mtorr and at 23 sccm. a. Deposition per cycle b. Film composition.

Figure 11. Overall deposition rate. a. Off-time data from Fig. 4a. b. On-time data from Fig. 10a. c. Duty Cycle

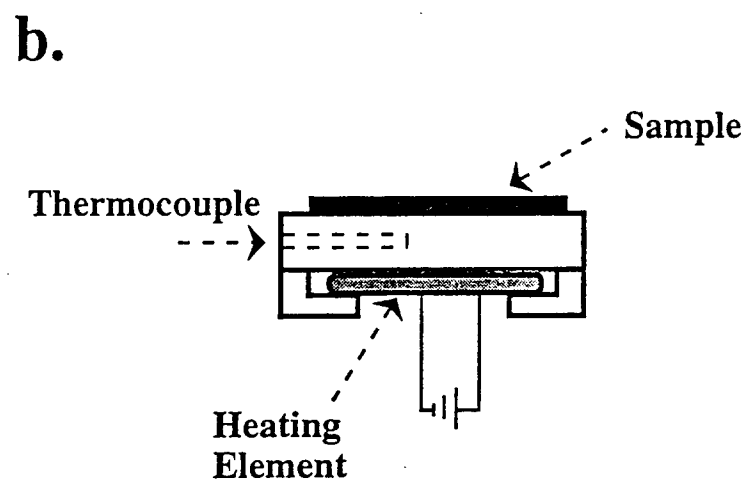
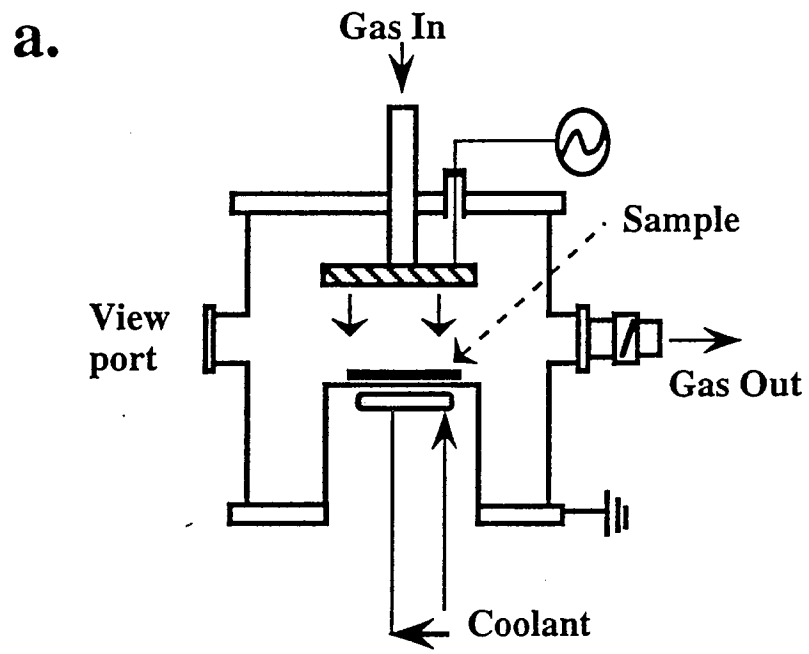
Figure 12. Defined control volume in-between the electrodes.

Figure 13. Comparison between the model predicted deposition per cycle and the experimental data. The parameter values in Table 2 were used in the model. a. Case 1.  
b. Case 2.

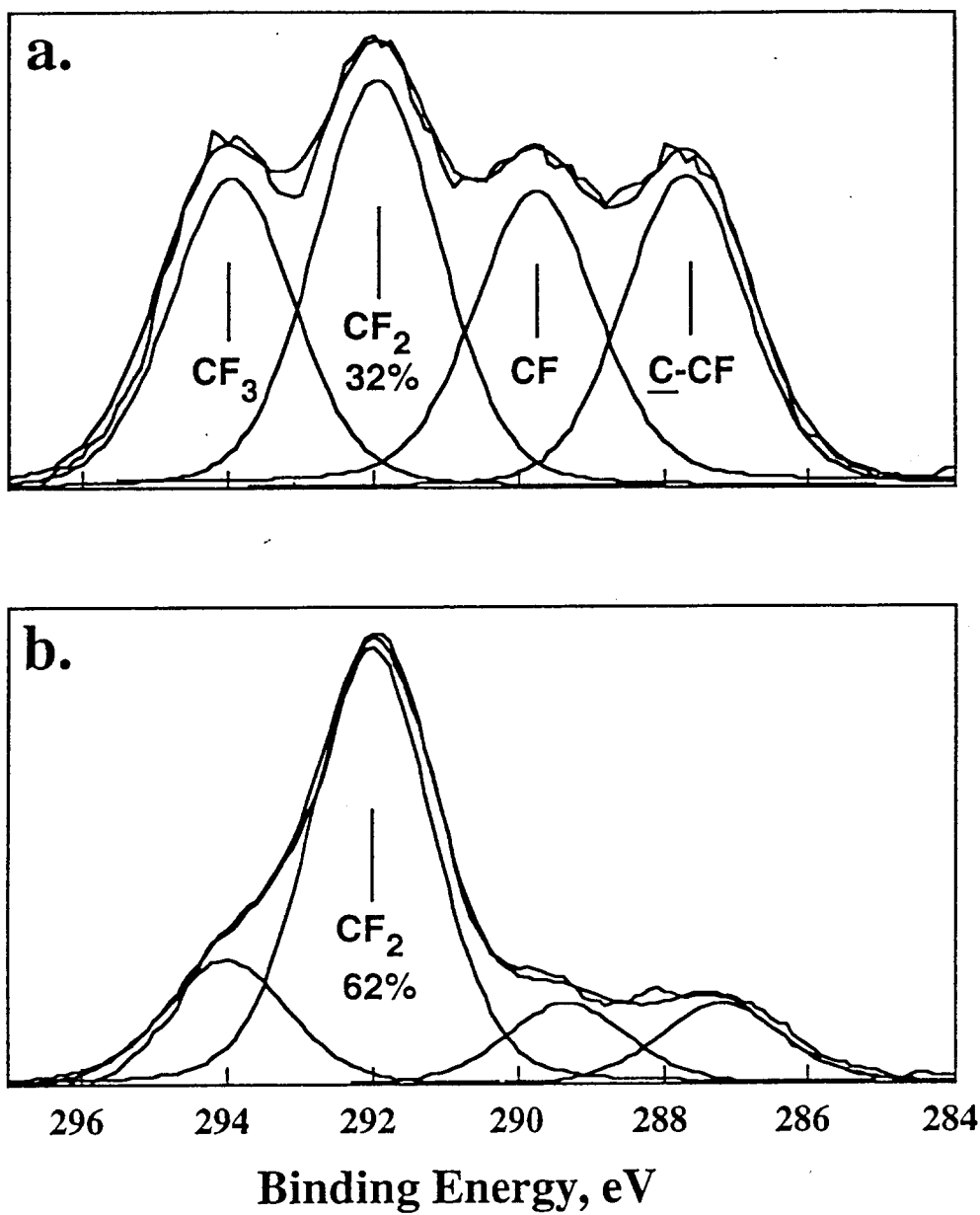
Figure 14. Predicted  $CF_x$  concentration during the on-time.

Figure 15. Predicted  $G_{on}$  as a function of on-time at 1000 mtorr and 12.5 sccm. a. On-time between 0 to 7000 ms. b. On-time between 0 to 100 ms.

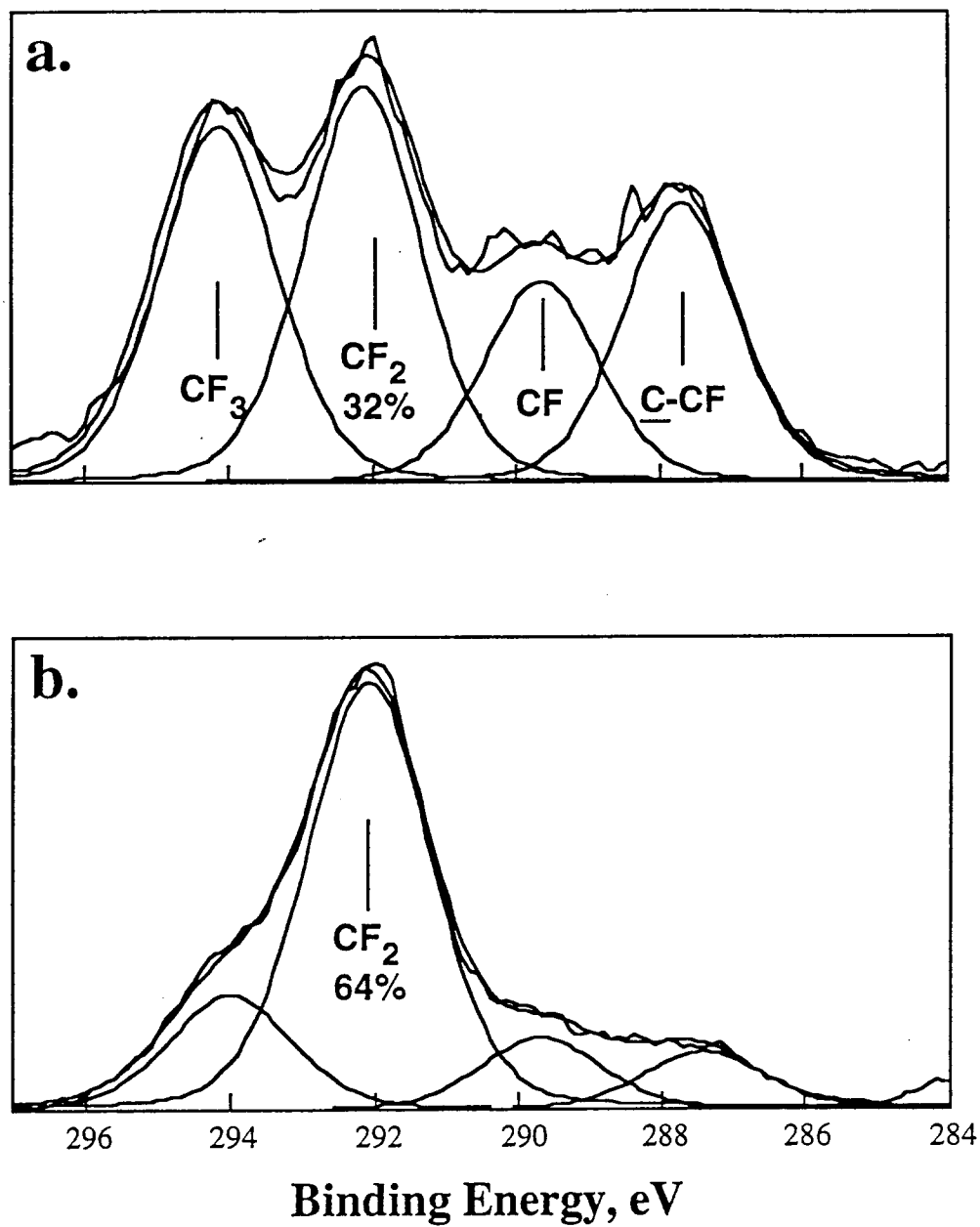
Figure 16. Predicted deposition per cycle data in comparison with experimental data.



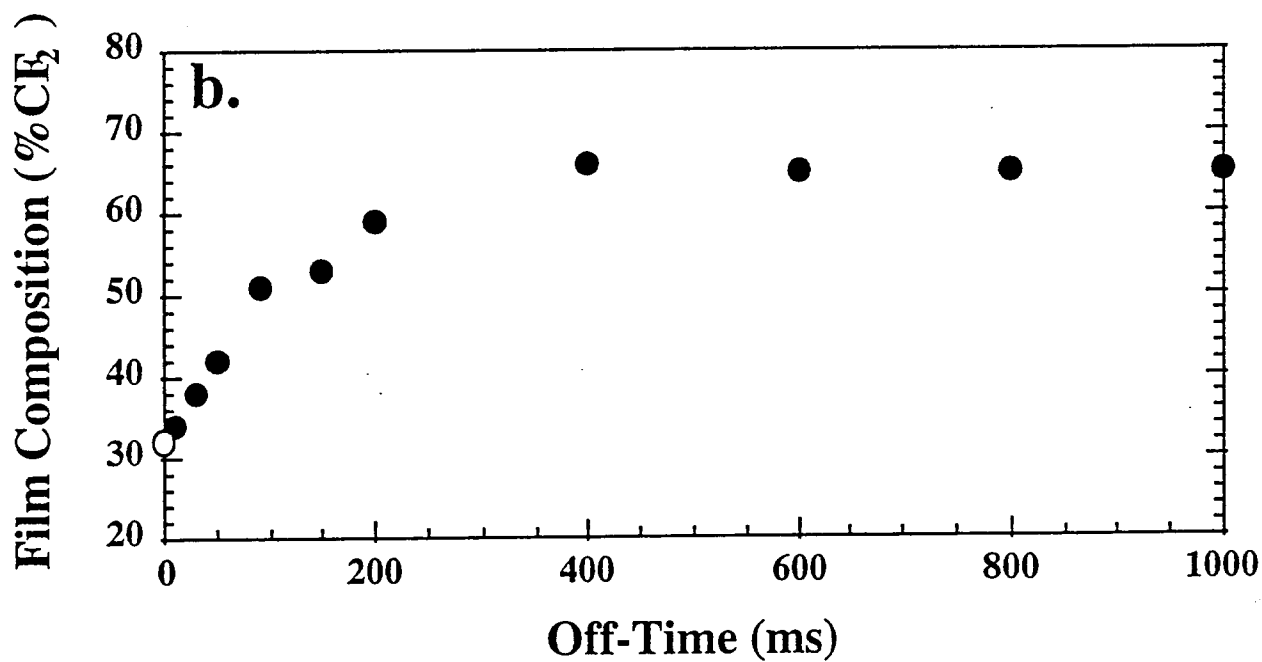
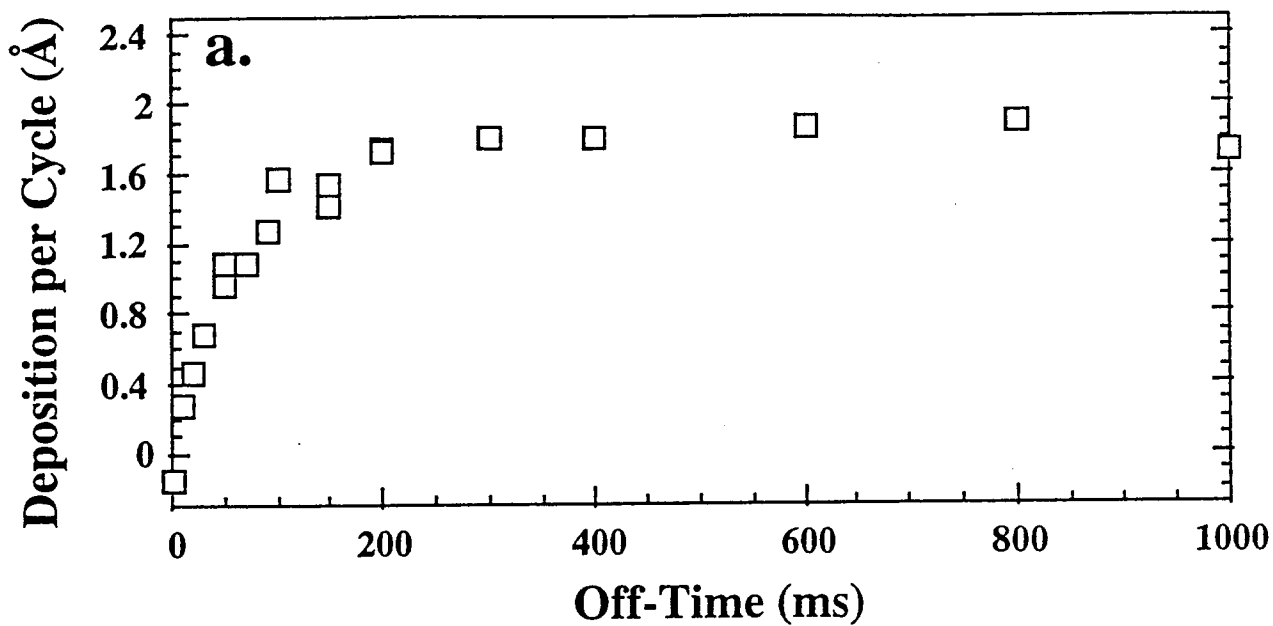
Scott J. Limb Figure 1.



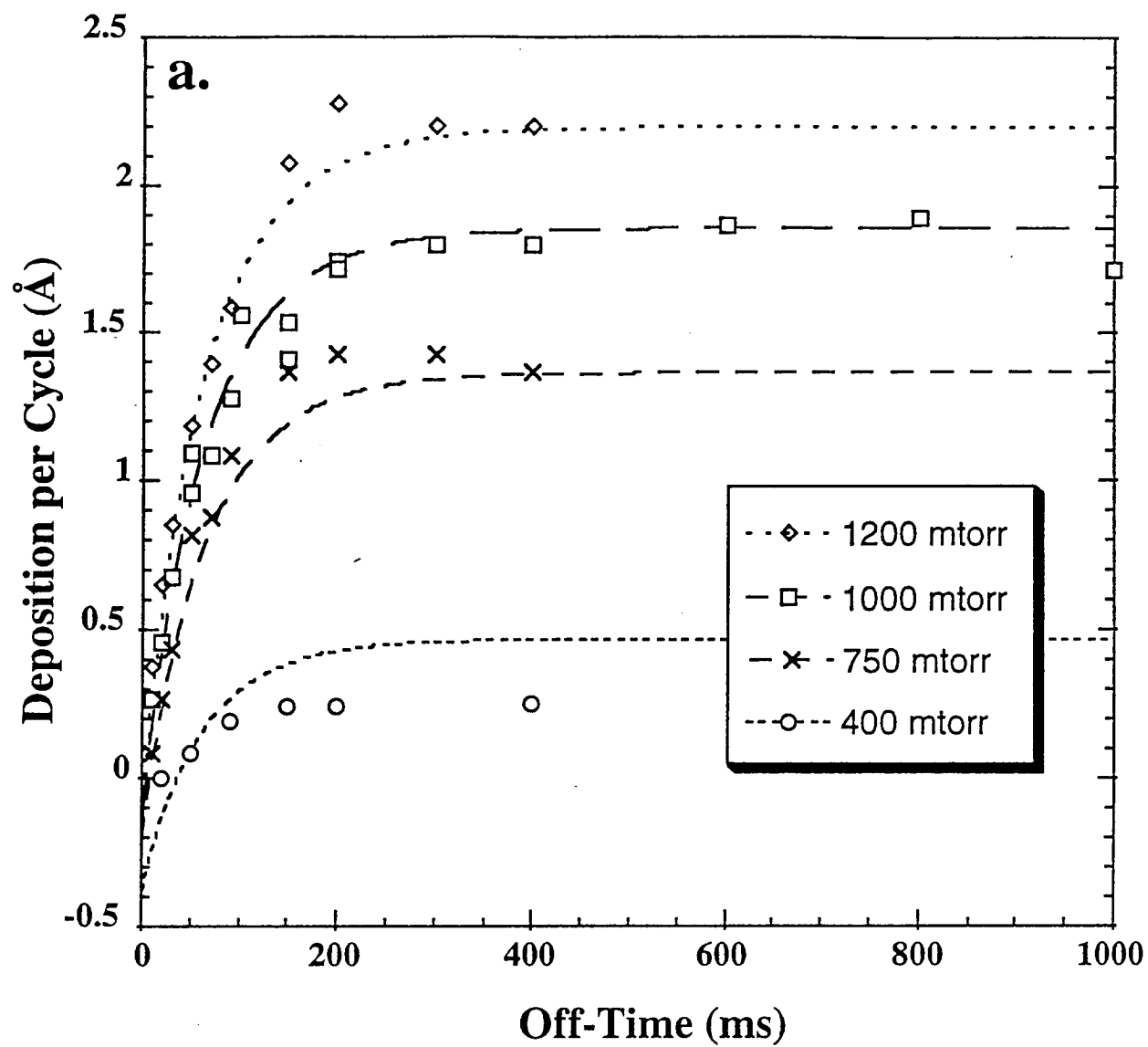
Scott J. Limb, Figure 2.



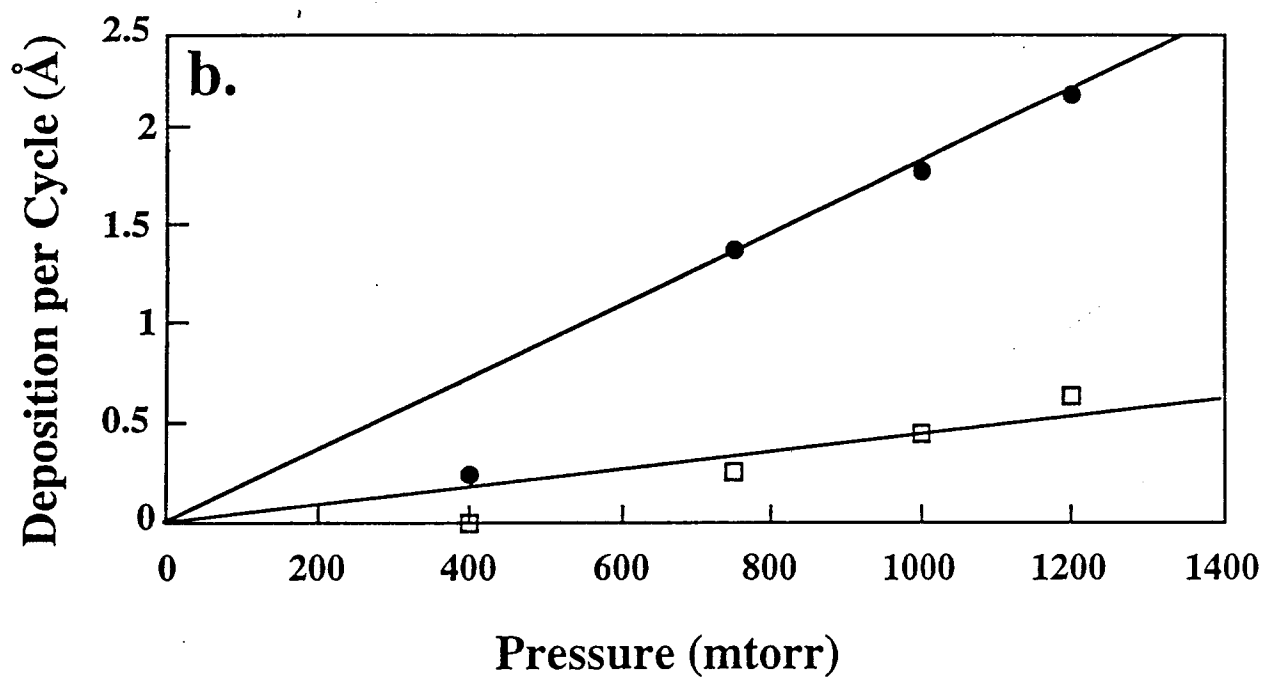
Scott J. Limb, Figure 3.



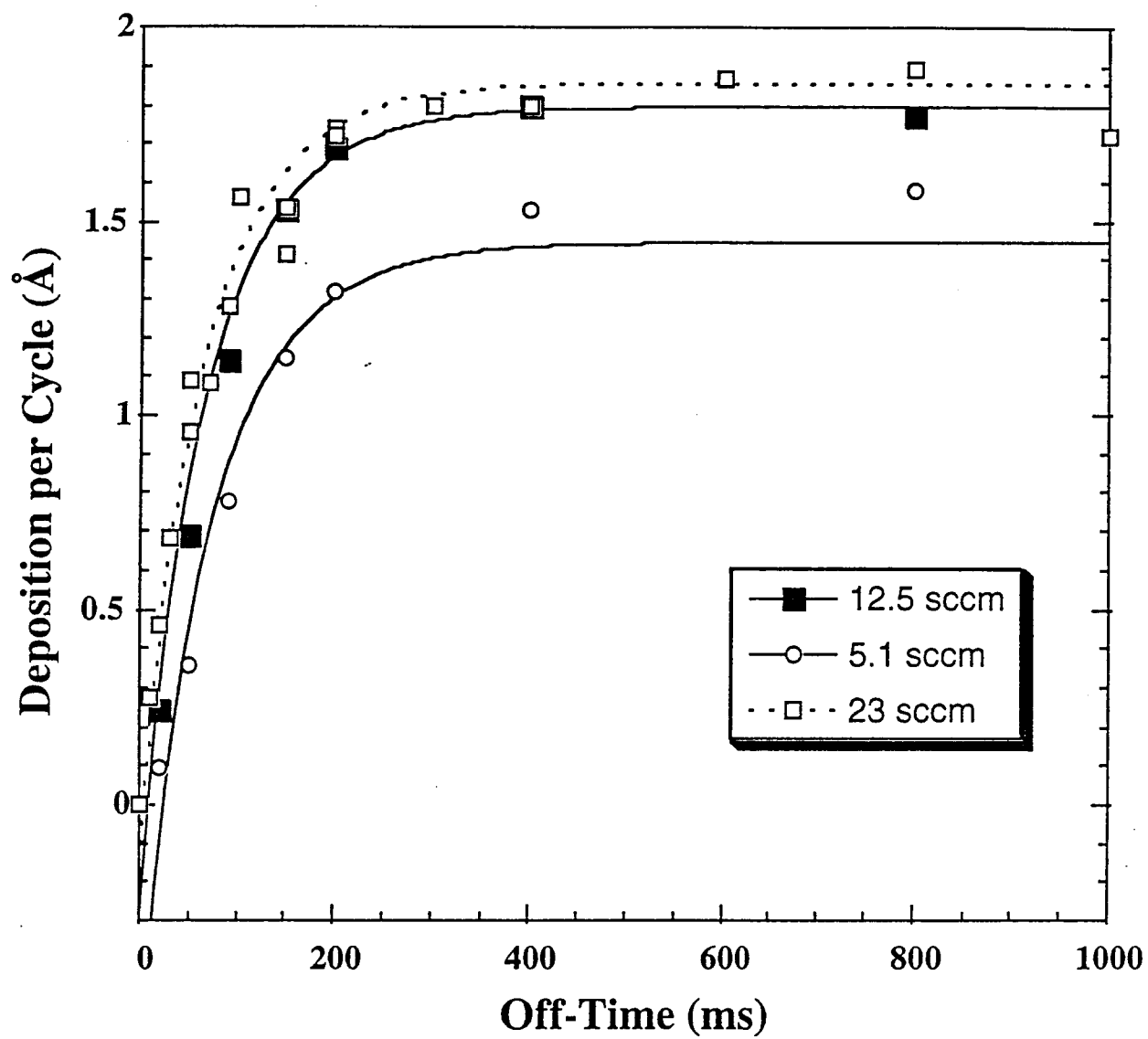
Scott J. Limb, Figure 4.



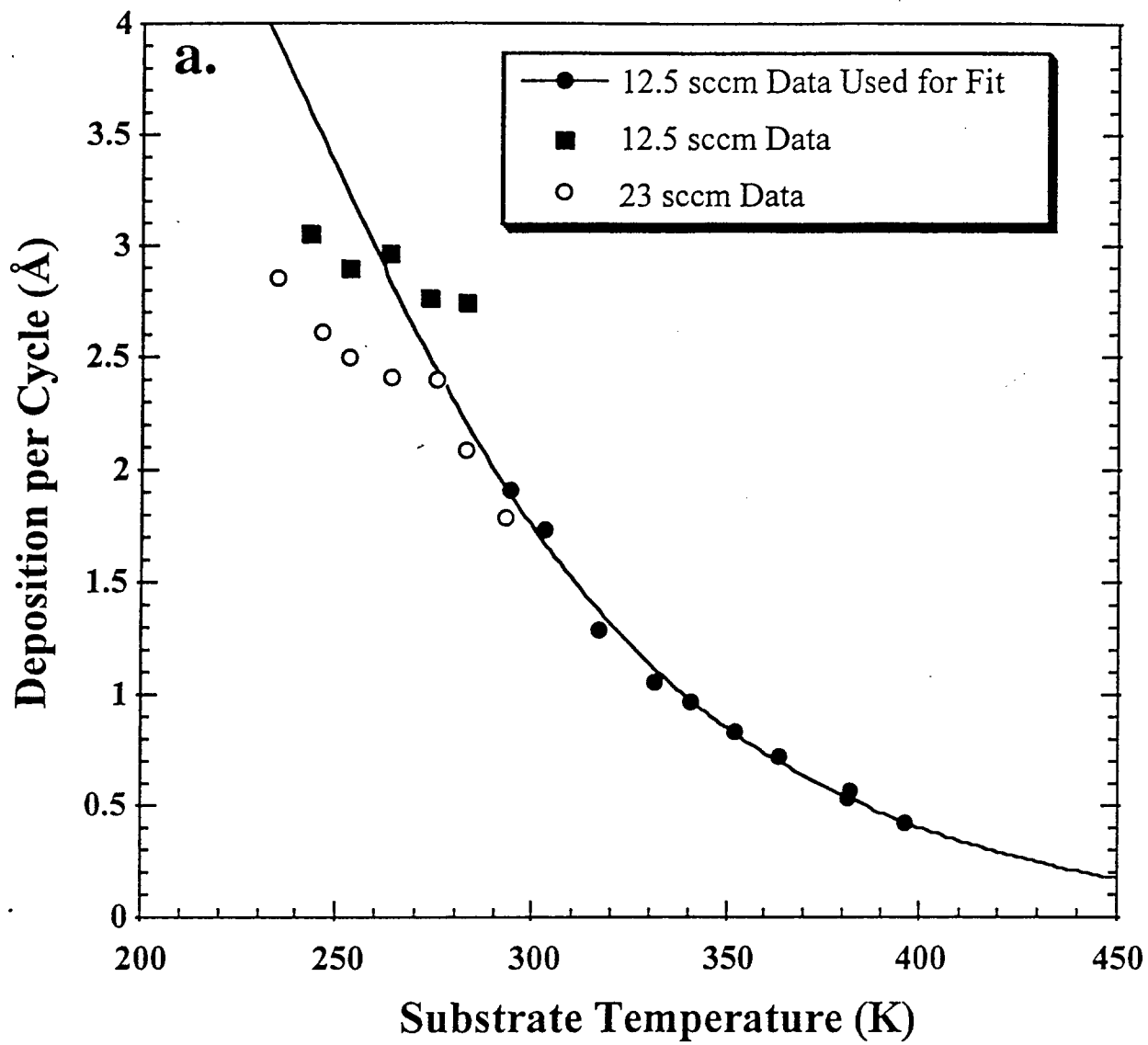
Scott J. Limb, Figure 5a.



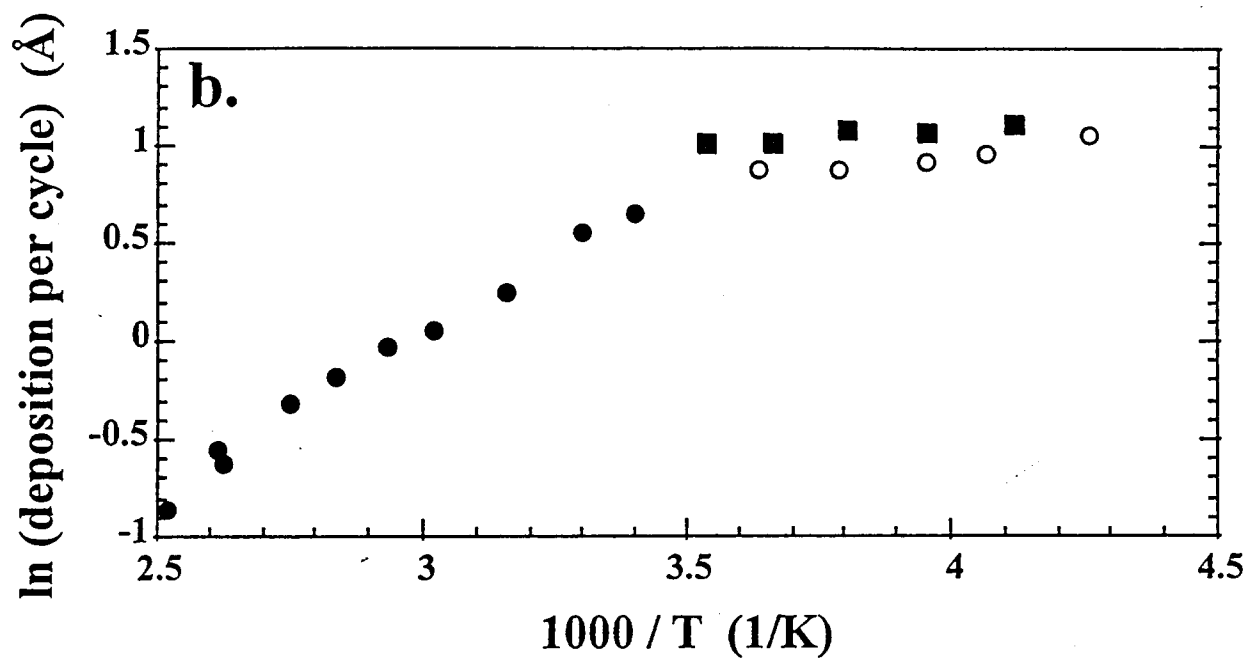
Scott J. Limb, Figure 5b.



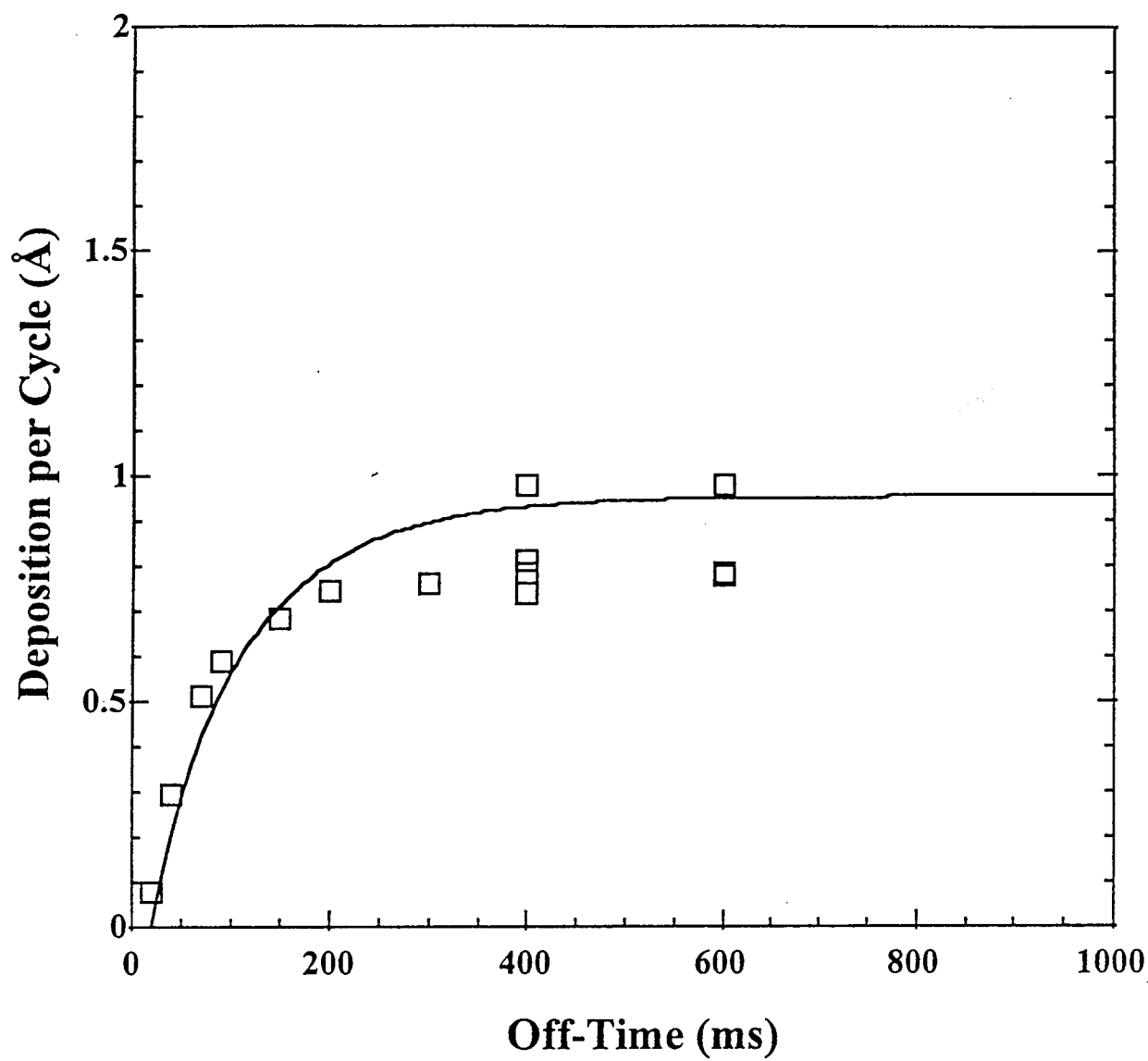
Scott J. Limb, Figure 6.



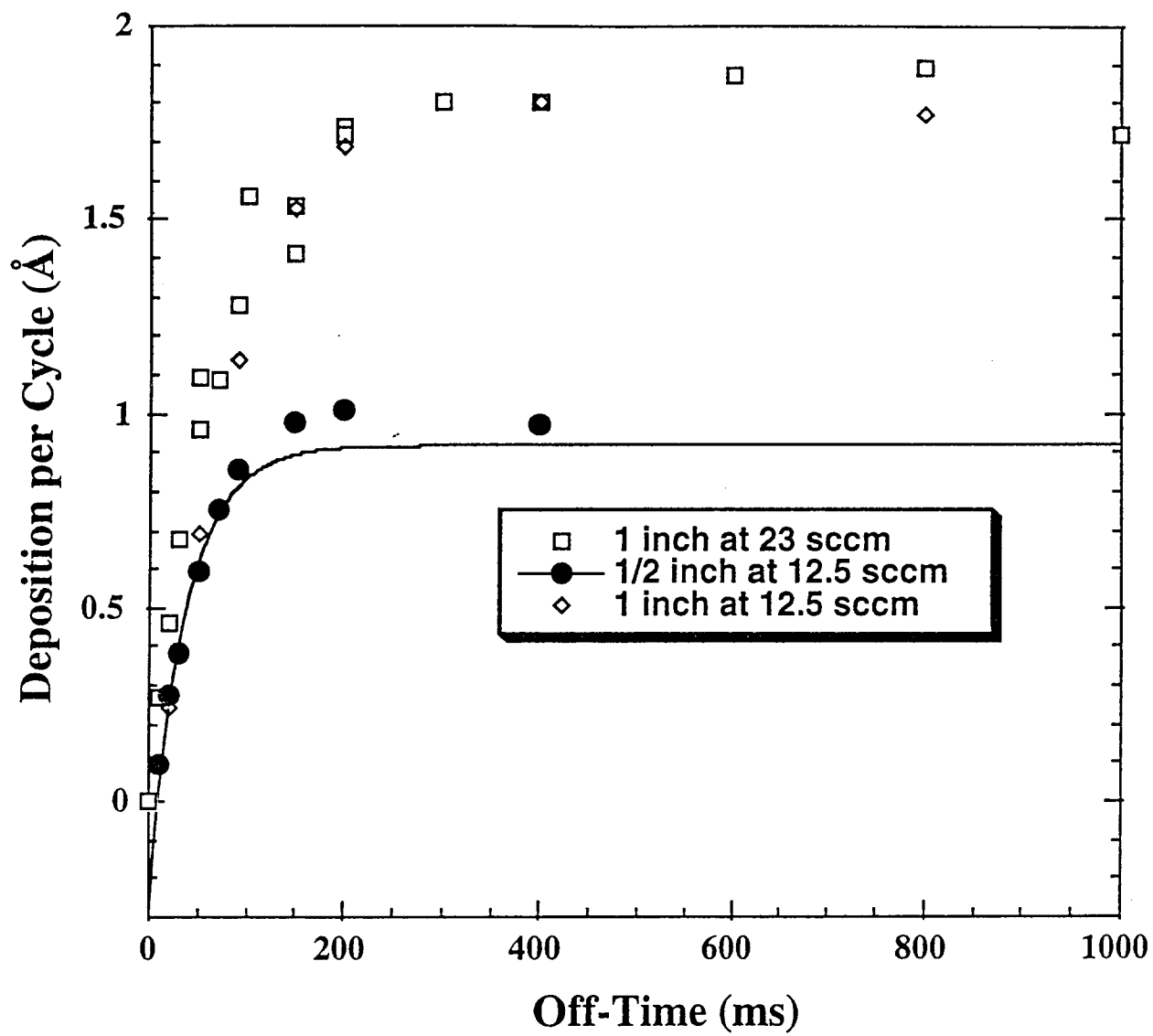
Scott J. Limb, Figure 7a.



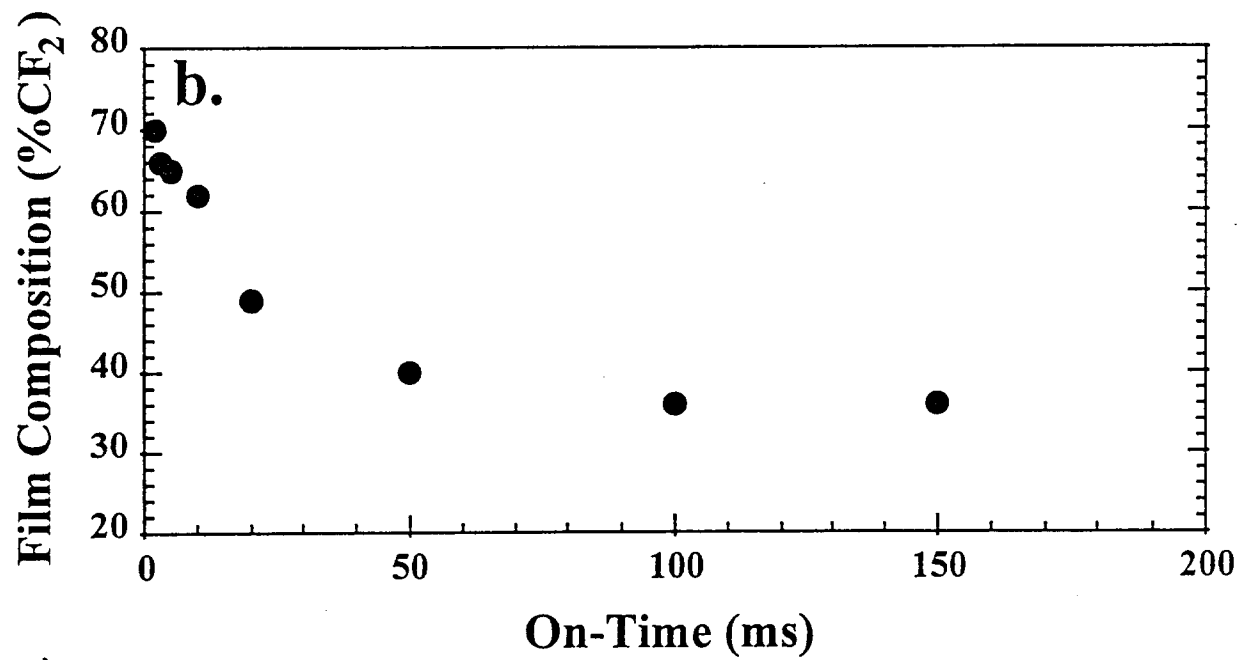
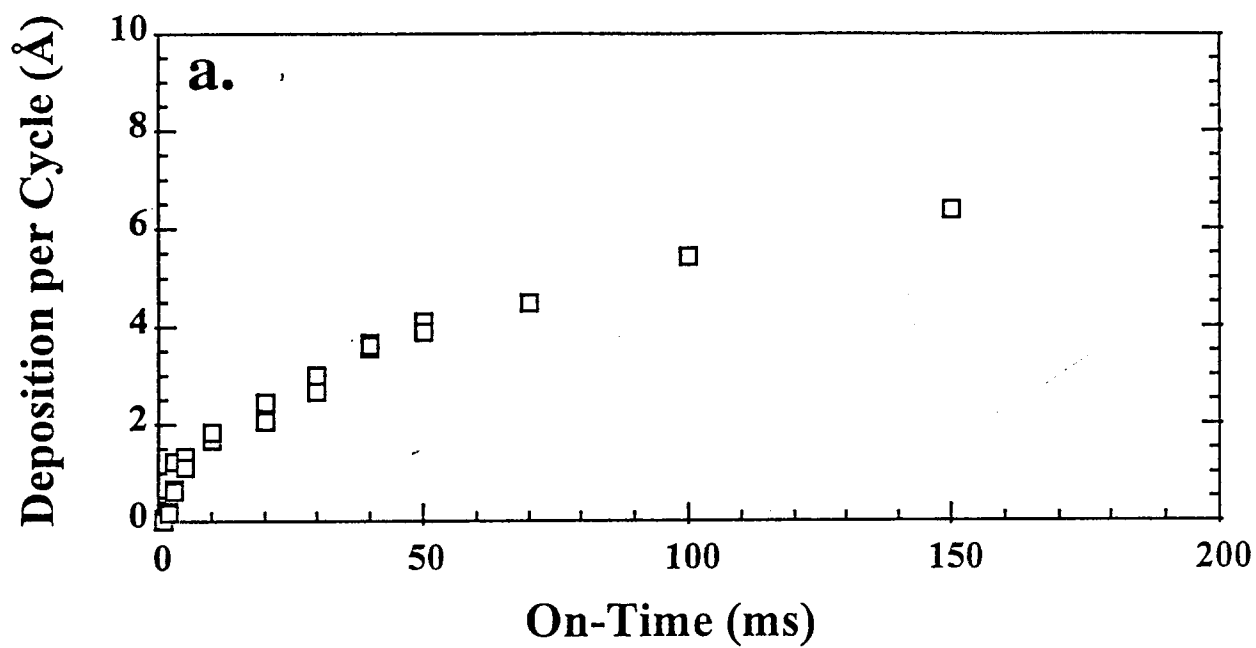
Scott J. Limb, Figure 7b.



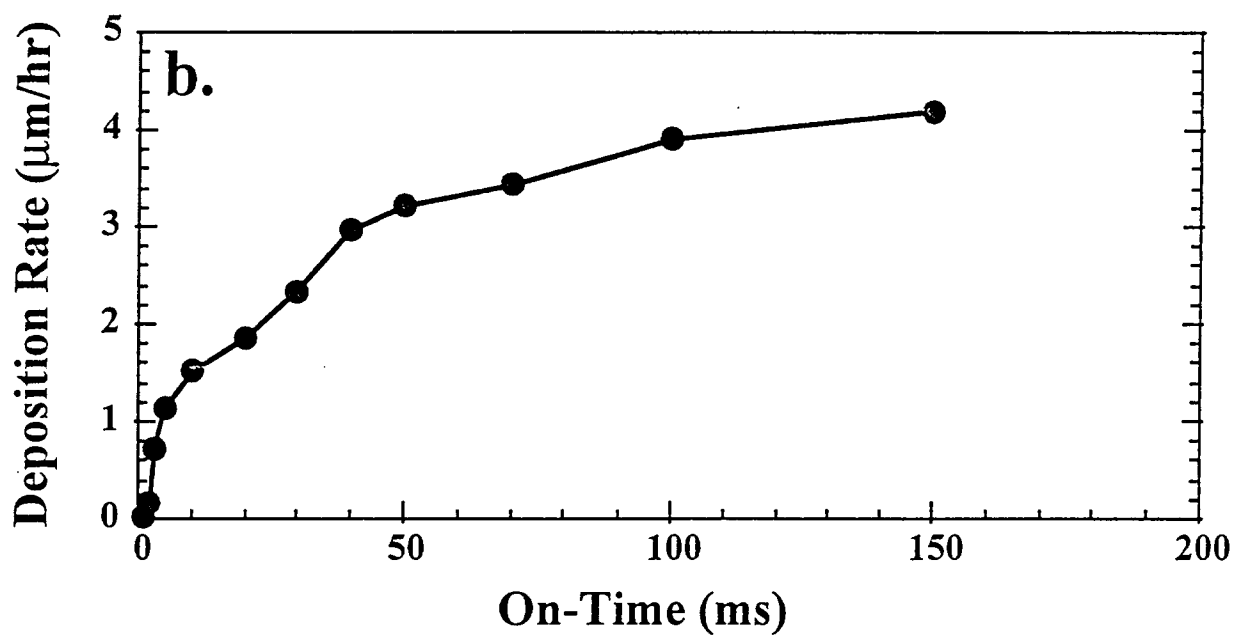
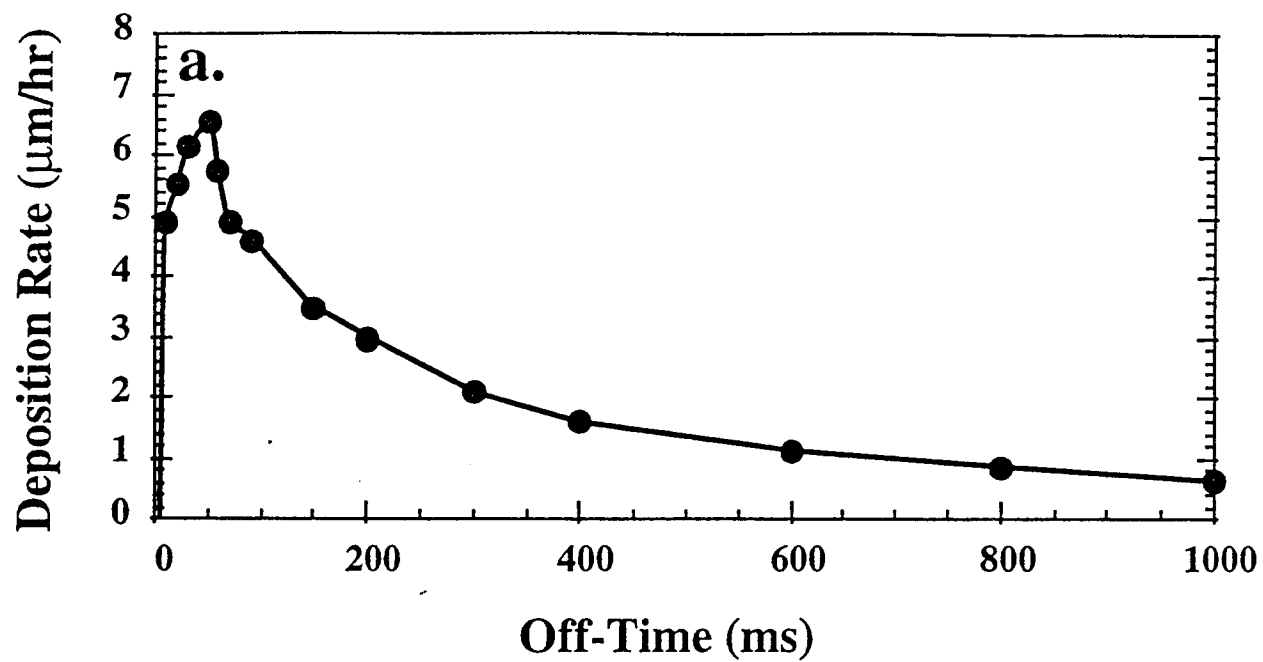
Scott J. Limb, Figure 8.



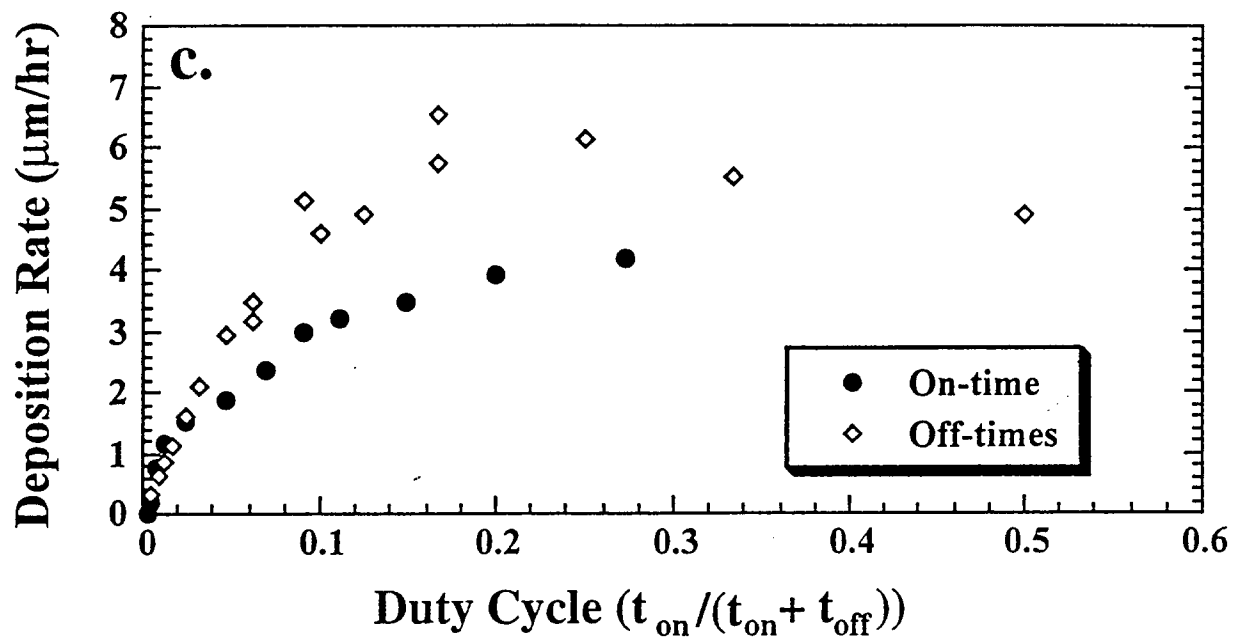
Scott J. Limb, Figure 9.

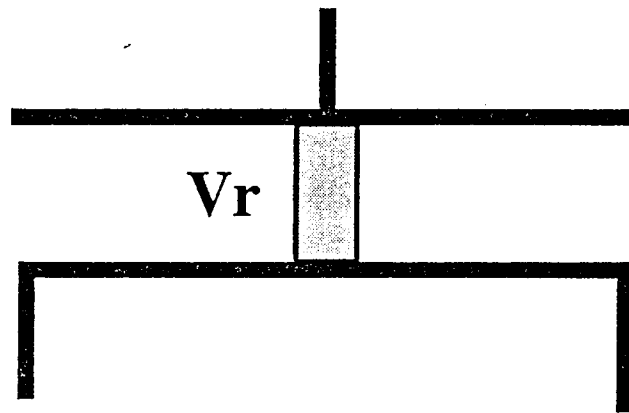


Scott J. Limb, Figure 10

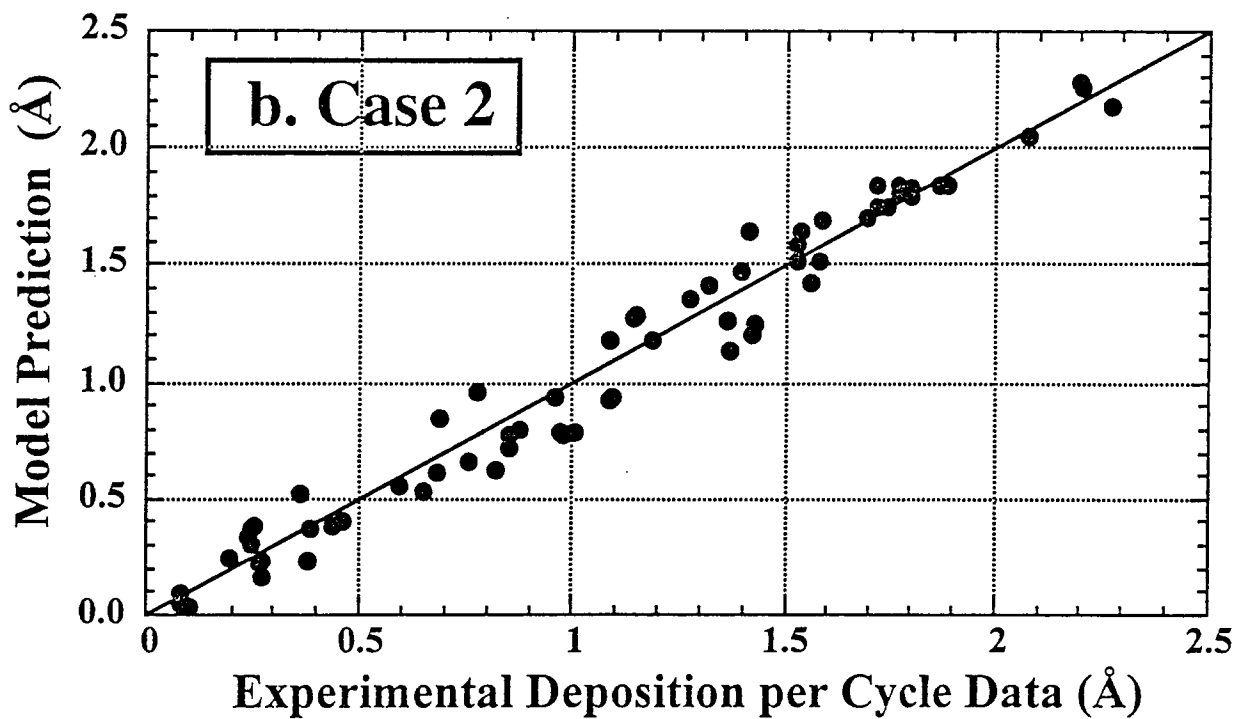
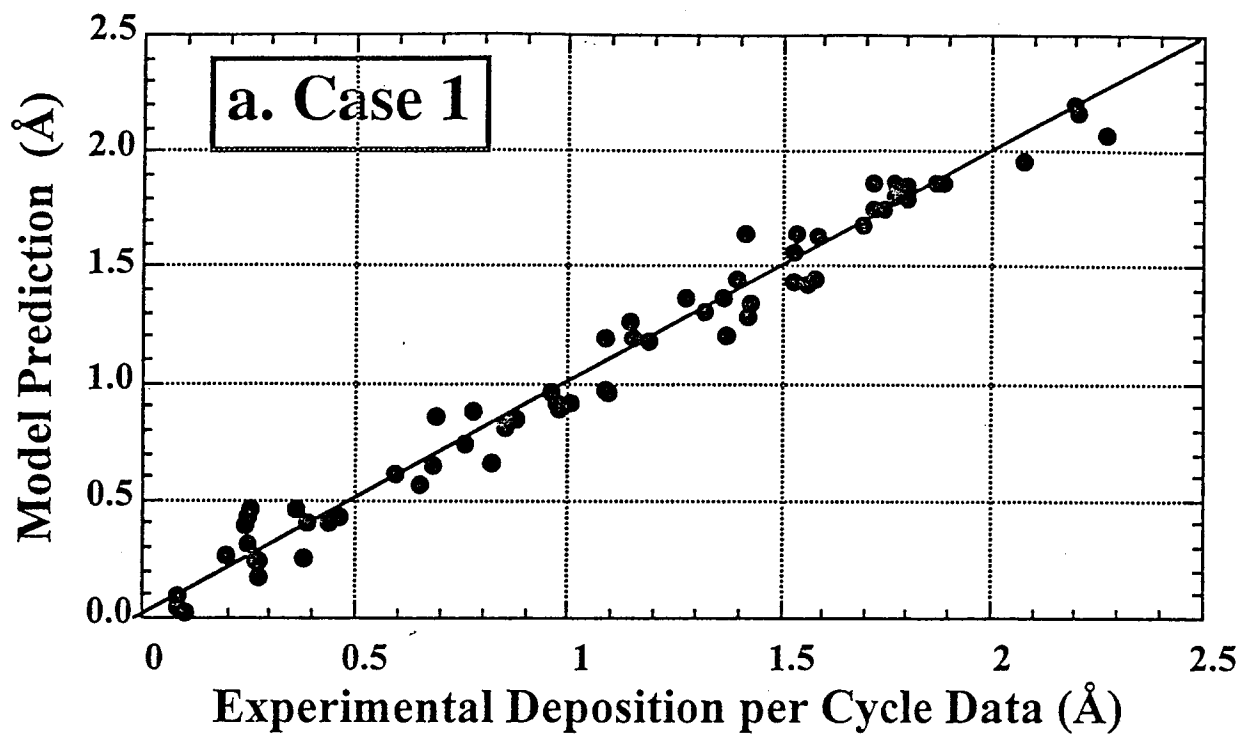


Scott J. Limb, Figure 11ab.

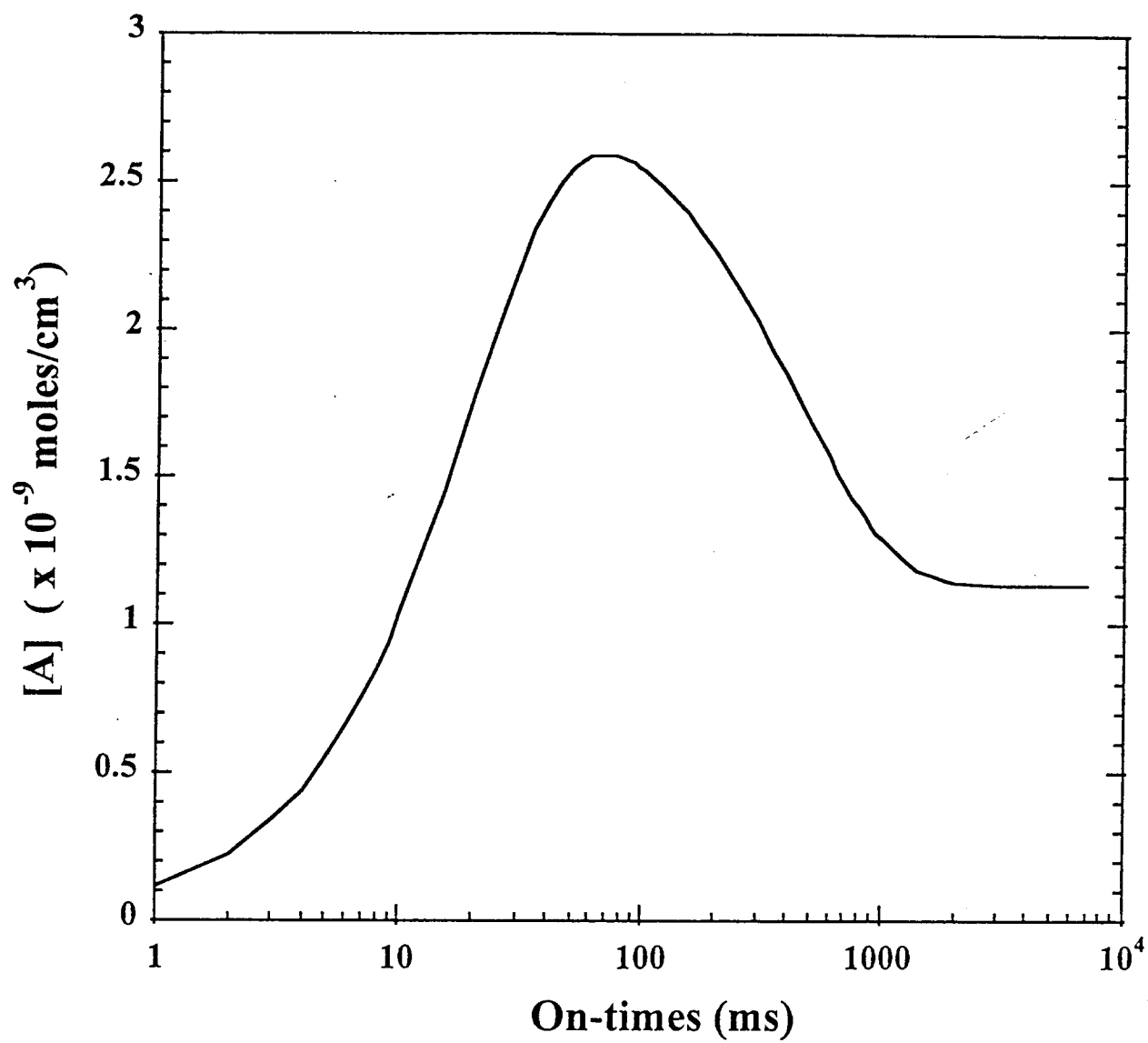




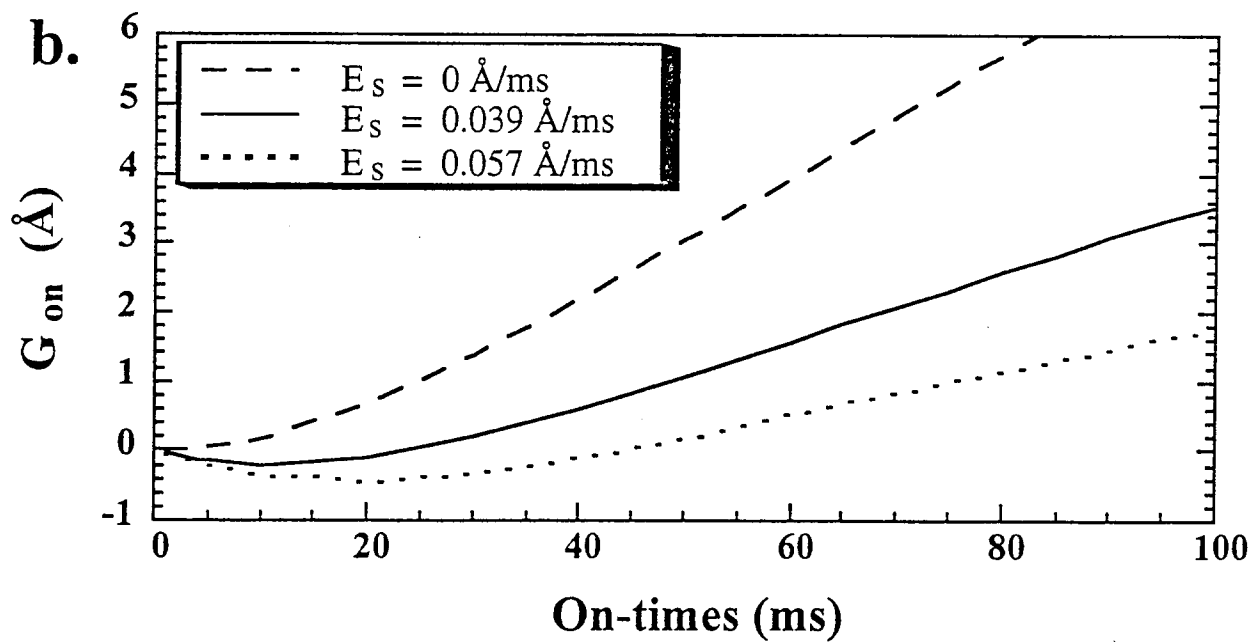
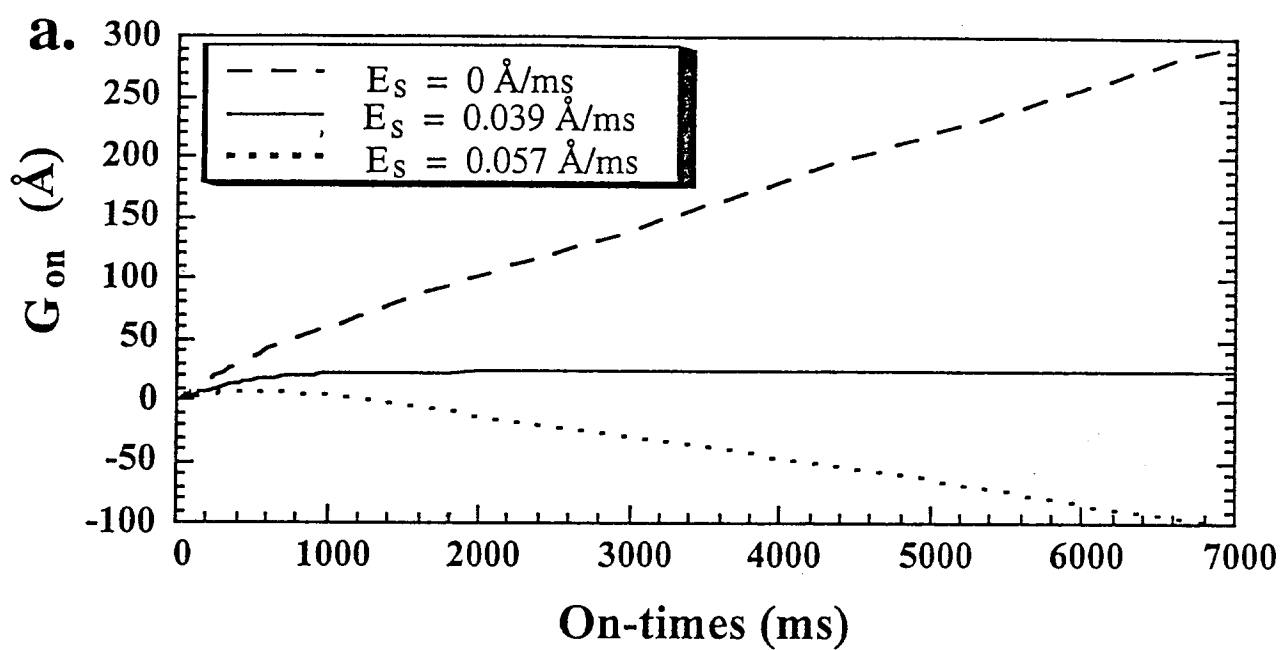
Scott J. Limb, Figure 12.

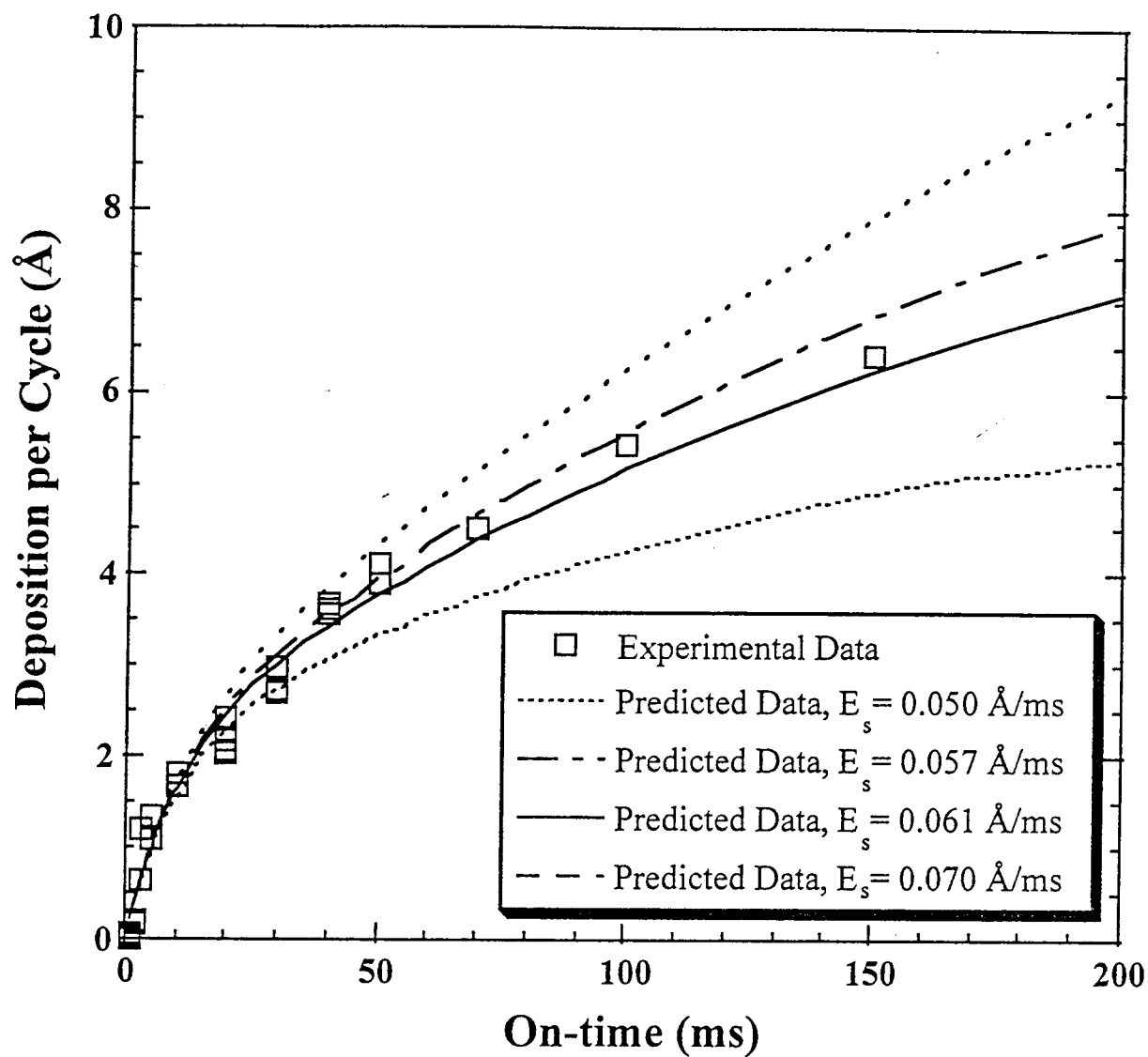


Scott J. Limb, Figure 13ab.



Scott J. Limb, Figure 14.





Scott J. Limb, Figure 16.